

To appear in Philosophical Transactions of the Royal Society A, doi: 10.1098/rsta.2024.0203.

Lagrangian approach to origami vertex analysis: Kinematics

Matthew Grasinger,^{*} Andrew Gillman, and Philip Buskohl[†]

Materials & Manufacturing Directorate, Air Force Research Laboratory

Abstract

The use of origami in engineering has significantly expanded in recent years, spanning deployable structures across scales, folding robotics, and mechanical metamaterials. However, finding foldable paths can be a formidable task as the kinematics are determined by a nonlinear system of equations, often with several degrees of freedom. In this work, we leverage a Lagrangian approach to derive reduced-order compatibility conditions for rigid-facet origami vertices with reflection and rotational symmetries. Then, using the reduced-order conditions, we derive exact, multi-degree of freedom solutions for degree 6 and degree 8 vertices with prescribed symmetries. The exact kinematic solutions allow us to efficiently investigate the topology of allowable kinematics, including the consideration of a self-contact constraint, and then visually interpret the role of geometric design parameters on these admissible fold paths by monitoring the change in the kinematic topology. We then introduce a procedure to construct lower symmetry kinematic solutions by breaking symmetry of higher order kinematic solutions in a systematic way that preserves compatibility. The multi-degree of freedom solutions discovered here should assist with building intuition of the kinematic feasibility of higher degree origami vertices and also facilitate the development of new algorithmic procedures for origami-engineering design.

I. INTRODUCTION

The use of origami principles in engineering has grown rapidly, highlighting its broad utility, versatility, and elegance. The scale invariance of these principles has led to the adoption of origami design at length scales as large as deployable space structures [1, 2] and shelters [3, 4], to smaller-scale biomedical applications [5–8], nanorobotics [9], and nanoscale devices [10, 11]. Besides deployable structures both big and small, the programmable shape transformations achievable with origami are amenable for driving locomotion in robotics [12–15], storing mechanical energy [16, 17] and mechanical information [18–20]. Further, because of the intricate connection between “form” and “function”, origami is a powerful tool for developing metamaterials with tunable thermal [21], mechanical [22–31] or electromagnetic [32] responses.

Techniques and algorithms have been developed for designing an origami crease pattern with particular kinds of mechanisms [33–36], or which, upon folding, approximates a given surface [17, 37–46]. Similarly, path finding methods have been developed for planning the deployment, locomotion, etc., of an origami structure given its fold pattern, and initial and final states of interest [47–49]. Underlying these tools are mathematical and computational models for the *forward* problem; that is, models for the kinematics of an origami structure that answer: “given a crease pattern, how does it fold?”.

Various computational techniques have been developed for the forward problem, each with different trade-offs in efficiency, accuracy, and complexity. Approaches utilizing continuum solid, shell and (higher-order) frame finite elements have been proposed [50–52]. These methods offer a high degree of accuracy, but at greater computational expense. Meanwhile bar-hinge-type models have emerged as alternatives that retain an engineering accuracy, but are more efficient and scalable [53–58]. The fundamental idea of bar-hinge models is to

* matthew.grasinger.1@us.af.mil

† philip.buskohl.1@us.af.mil

characterize the creases as structural bar elements with both axial and torsional stiffnesses, which model the elasticity of the faces and folding about the creases, respectively. The bar elements are then pin connected at the vertices of the origami, resulting in a Maxwell frame. One way to reduce the dimensionality of the model is to idealize the faces of the origami structure as rigid. This can be a good approximation when the stiffness of the faces is much larger than the torsional stiffness of the creases. Bar-hinge type models can model rigid-facet origami by constraining the bars to be rigid [59, 60]; and such an approach has been used for investigating the branches of folding motion off the flat state [59] and the influence of hidden symmetries in periodic origami structures [60]—as well as other origami problems of interest.

Assuming the faces of an origami structure are rigid leads to a condition on the fold angles of an origami structure such that it can be folded compatibly (i.e. without tearing). Given a counterclockwise, closed path on the origami structure, which does not intersect any vertices, the *loop-closure constraint* says that the product of the rotation matrices corresponding with each of the creases traversed by the path must be the identity matrix [61]. Tachi [48] developed a method for computational origami folding by linearizing the constraint about a given, folded state. Then all allowable perturbations to the fold angles can be formulated as a linear system of equations. Wu and You [62] proposed a model, also based on the loop-closure constraint, that utilized quaternions and dual-quaternions. An efficient, alternative method was introduced in Zhou et al. [47] with a redundant kinematic description, including both vertices and faces, that instead used a global constraint for ensuring vertices coincided with the corners of their respective facets. Other notable work for the forward problem includes continuum theories which coarse grain over the fold pattern to model origami as elastic continua (e.g. plates) [63–65].

While these computational methods offer many advantages, there are still several reasons that closed-form, analytical solutions are of interest. Inverse design and optimization strategies generally rely on efficient forward models in order to be feasible. Unsurprisingly, many of the design algorithms that are among the most efficient, and are rigorously proven to work for general problems, are based on the well-known, exact solution for degree 4 origami vertices (i.e. vertices where 4 creases meet), and are restricted to quadrilateral origami. Insight gained from analytical solutions can also be used to develop and discover new design heuristics and algorithms. What appears to be the first analytical solution of origami kinematics was derived in a seminal paper by Huffman [66]. For a closed-path on a surface, the Gauss map produces a corresponding path on the unit sphere by taking the trace of the surface normal as it changes along the (surface) path. Huffman appealed to the Gauss map for a degree 4 vertex, then had the remarkable insight to use invariants of the path along with spherical trigonometry to derive implicit relationships between the fold angles. Similar derivations, based on spherical trigonometry, were later performed by Hanna et al. [67] to obtain an explicit solution for the folding of the symmetric 8 fold waterbomb. The resulting equations were later simplified [29] and generalized to other variants of the waterbomb [68].

An alternative approach for finding analytical solutions has roots in [61] where the loop-closure constraint was derived by modeling the folded state of origami using affine transformations. There it was recognized that the deformation of the origami could be described by products of rotations. Later work recognized the connection between these affine transformations and fundamental concepts in continuum solid mechanics such as the deformation map, the deformation gradient, and Lagrangian approaches to kinematics [37, 38, 45, 69]. The authors used this perspective to obtain a simplified solution for degree 4 vertices [37, 38];

and, more importantly, 1) demonstrated that it could be combined with concepts from objective structures [70] and group theory to efficiently generate folded states of helical origami structures [38], and 2) developed a rigorous origami design algorithm for approximating surfaces [37]. In [71], the authors use a similar, Lagrangian-like approach to derive explicit kinematic equations for general, rigid-facet degree 4 vertices, both Euclidean and non-Euclidean (i.e. sector angles sum to 2π and do not sum to 2π , respectively; non-Euclidean origami cannot be flat without facet deformation or tearing). This work was later extended to consider various folding motions of the fully symmetric degree 6 vertex (i.e. the degree 6 vertex in which all of the sector angles are $\pi/3$) [72]. Other notable analytical and rigorous results have been obtained for the hyperbolic paraboloid, or “hypar”, origami regarding conditions for its foldability, parameterization of its surface during folding, and its bistability [73, 74].

With very few exceptions, past work on obtaining exact solutions to the folding of rigid-facet origami has been restricted to single degree of freedom solutions. Here, inspired by past work leveraging both group theory and the Lagrangian approach to origami, we derive reduced-order compatibility conditions for origami vertices with reflection and rotational symmetries. The Lagrangian approach is outlined in section II, followed by a first example in section III. Then, using the reduced-order conditions, exact, multi degree of freedom solutions are obtained for degree 6 and degree 8 vertices with reflection (section IV) and reflection-rotation (section V) symmetries. We then introduce a procedure to construct lower symmetry kinematic solutions by breaking symmetry of higher order kinematic solutions in a systematic way that preserves compatibility. The work concludes in section VI.

II. THE LAGRANGIAN APPROACH FOR ORIGAMI KINEMATICS

Often in practice with origami, the object being folded is “thin enough” (e.g. paper) such that its bending stiffness is much less than its stiffness with respect to in-plane stretching. Further, the bending stiffness of its facets is often much larger than the torsional stiffness of the creases. As a result, creases represent the preferred means of deformation, and, to a good approximation, we can idealize the deformation of the structure as occurring strictly through rotations of its facets about its creases. Because the facets are assumed rigid, one finds that the group of orthogonal linear transformations, $O(3) = \{\mathbf{L} \in GL(3) : \mathbf{L}^T = \mathbf{L}^{-1}\}$, is a powerful tool for mapping flat origami crease patterns into folded states (see, for example, [37, 38, 61, 69]). Before outlining the Lagrangian approach, we introduce the following notation:

- Ω_0 and Ω denote the body of the origami in the reference and deformed (i.e. folded) configurations, respectively.
- $\mathbf{x} \in \Omega_0$ and $\mathbf{y} \in \Omega$ denotes positions in the reference and deformed configurations, respectively.
- $\Phi : \mathbf{x} \mapsto \mathbf{y}$ denotes the deformation map (or fold map), i.e. $\mathbf{y} = \Phi(\mathbf{x})$.
- \mathbf{F} denotes the deformation gradient, $\mathbf{F} = \text{Grad } \Phi$ or $[\mathbf{F}]_{ij} = \partial y_i / \partial x_j$.
- $\sigma_{\hat{\mathbf{u}}} \in O(3)$ denotes a reflection about the plane which passes through the origin and is orthogonal to $\hat{\mathbf{u}}$;

$$\sigma_{\hat{\mathbf{u}}} = \mathbf{I} - 2\hat{\mathbf{u}} \otimes \hat{\mathbf{u}}, \quad (1)$$

where $\mathbf{u} \otimes \mathbf{v}$ denotes the outer product of \mathbf{u} and \mathbf{v} such that $(\mathbf{u} \otimes \mathbf{v})_{ij} = u_i v_j$.

- $\mathbf{Q}_{\hat{\mathbf{u}}}(\varphi) \in SO(3) \leq O(3)$ denotes a rotation of φ radians about the axis $\hat{\mathbf{u}}$; i.e.

$$\mathbf{Q}_{\hat{\mathbf{u}}}(\varphi) = \exp(\varphi \mathbf{A}_{\hat{\mathbf{u}}}) = (1 - \cos \varphi) \hat{\mathbf{u}} \otimes \hat{\mathbf{u}} + \cos \varphi \mathbf{I} + \sin \varphi \mathbf{A}_{\hat{\mathbf{u}}}, \quad (2)$$

where

$$\mathbf{A}_{\hat{\mathbf{u}}} := \begin{pmatrix} 0 & -\hat{u}_3 & \hat{u}_2 \\ \hat{u}_3 & 0 & -\hat{u}_1 \\ -\hat{u}_2 & \hat{u}_1 & 0 \end{pmatrix} \quad (3)$$

is the skew-symmetric transformation such that $\mathbf{A}_{\mathbf{u}}\mathbf{v} = \mathbf{u} \times \mathbf{v}$ for all $\mathbf{v} \in \mathbb{R}^3$, and $SO(3) = \{\mathbf{L} \in O(3) : \det \mathbf{L} = 1\}$ is the group of special orthogonal transformations.

In this work, we will restrict our attention to a single origami vertex. Towards describing a folded deformation, start with any crease, label it 1, and then proceed around the vertex in the counterclockwise direction, labeling each subsequent crease, 2, 3, \dots , N , where N is the number of creases at the vertex. Then let the unit vector which begins at the vertex and extends along crease i in the reference configuration be denoted by \mathbf{b}_i . The reference configuration is chosen to be the flat state throughout. Further, $\phi_i \in [-\pi, \pi]$ denotes the supplement of the dihedral angle between the faces adjacent to crease i and is referred to as the *fold angle* at crease i . For the facets, let the facet which is bounded by the creases i and $i + 1$ be denoted by $\Omega_0^{(i)}$ and $\Omega^{(i)}$ in the reference configuration and deformed configuration, respectively, for $i = 1, \dots, N - 1$; similarly, $\Omega_0^{(N)}$ and $\Omega^{(N)}$ is the facet bounded by the creases N and 1. As is often the case in solid mechanics, we are only interested in the deformation map up to rigid body rotations and translations so without loss of generality assume that $\Omega^{(N)} = \Omega_0^{(N)}$ is fixed. Then it is easy to see that $\mathbf{y} = (\mathbf{Q}_{\hat{\mathbf{b}}_1}(\phi_1)) \mathbf{x}$ for $\mathbf{x} \in \Omega_0^{(1)}$. Similarly, because by assumption there are no tears and thus $\Omega^{(1)}$ is joined to $\Omega^{(2)}$ at crease 2, we have that $\mathbf{y} = (\mathbf{Q}_{\hat{\mathbf{b}}_1}(\phi_1)) (\mathbf{Q}_{\hat{\mathbf{b}}_2}(\phi_2)) \mathbf{x}$ for $\mathbf{x} \in \Omega_0^{(2)}$. Generalizing this argument to all facets leads to the following result,

$$\mathbf{y} = \Phi(\mathbf{x}) = \left(\prod_{i=1}^j \mathbf{Q}_{\hat{\mathbf{b}}_i}(\phi_i) \right) \mathbf{x}, \quad \mathbf{x} \in \Omega_0^{(j)}, \quad (4)$$

As $\Phi(\mathbf{x})$ is a linear transformation of \mathbf{x} , the deformation gradient is simply

$$\mathbf{F}(\mathbf{x}) = \prod_{i=1}^j \mathbf{Q}_{\hat{\mathbf{b}}_i}(\phi_i), \quad \mathbf{x} \in \Omega_0^{(j)}, \quad (5)$$

which is piecewise constant. For brevity, let \mathbf{F}_i be defined such that $\Omega^{(i)} = \mathbf{F}_i \Omega_0^{(i)}$.

Recall that the above formulation of the deformation map assumes that 1) $\Omega_0^{(N)}$ is fixed and 2) there are no tears, i.e. the deformation is compatible. As a result, a necessary and sufficient condition ¹ for a compatible deformation is given by the loop-closure constraint [61]

$$\mathbf{F}_N(\phi_1, \dots, \phi_N) = \prod_{i=1}^N \mathbf{Q}_{\hat{\mathbf{b}}_i}(\phi_i) = \mathbf{I}. \quad (6)$$

¹ The condition is only necessary and no longer sufficient when facets are prohibited from passing through each other [61]; i.e., satisfying (6) alone does not guarantee that the origami vertex will not contact or intersect itself.

Choosing the deformation map from among the group of rigid body translations and rotations² of the origami such that $\mathbf{F}_N = \mathbf{I}$ is a standard convention which is convenient for deriving (6). However, in the proceeding sections we will adjust this convention based on the symmetry of the underlying crease pattern in order to simplify the reduced order compatibility conditions. For example, when considering vertices with reflection symmetry about the plane which cuts through crease 1, it will be convenient to adopt the convention

$$\begin{aligned} \mathbf{F}_1 &= \mathbf{Q}_{\hat{\mathbf{b}}_1} \left(\frac{\phi_1}{2} \right), \quad \mathbf{F}_2 = \mathbf{Q}_{\hat{\mathbf{b}}_1} \left(\frac{\phi_1}{2} \right) \mathbf{Q}_{\hat{\mathbf{b}}_2} (\phi_2), \quad \dots, \\ \mathbf{F}_N &= \mathbf{Q}_{\hat{\mathbf{b}}_1} \left(\frac{\phi_1}{2} \right) \prod_{i=2}^N \mathbf{Q}_{\hat{\mathbf{b}}_i} (\phi_i) = \mathbf{Q}_{\hat{\mathbf{b}}_1} \left(-\frac{\phi_1}{2} \right) \end{aligned} \quad (7)$$

which corresponds to rigidly rotating the body by $\mathbf{Q}_{\hat{\mathbf{b}}_1}(-\phi_1/2)$ and where the last equality corresponds to multiplying both sides of (6) by $\mathbf{Q}_{\hat{\mathbf{b}}_1}(-\phi_1/2)$. The exact choice of the deformation map will be made clear in each subsequent example provided.

While (6) is quite general, it is also highly nonlinear and difficult to solve except in special cases. In this work, we focus on vertices with various symmetries and find that the Lagrangian description facilitates leveraging those symmetries to reduce the complexity of the problem and obtain closed-form solutions.

III. A FIRST EXAMPLE: 4-VERTEX WITH REFLECTION SYMMETRY

We introduce the key ideas of the overarching approach by using degree 4 vertices as a first example. The 4 vertex has a single degree of freedom, but two separate kinematic folding solutions that bifurcate off of the flat configuration. The kinematics of degree 4 vertices are well-known [66, 71], so it presents a natural starting point for illustrating the approach proposed herein. The 4 vertices considered here have two collinear folds and a reflection symmetry about the axis which contains the collinear folds. This vertex is parameterized by a single parameter: the sector angle between the first two creases, α_1 . Let the coordinate system be such that the origin is at the vertex, the reflection symmetry is orthogonal to the $\hat{\mathbf{e}}_2$ direction, and the $\hat{\mathbf{e}}_3$ direction is orthogonal to the flat configuration. The geometry of the vertex and choice of coordinate system are shown in fig. 1.

An important observation from fig. 1 is that the flat state can be constructed by starting with $\Omega_0^{(1)}$ and $\Omega_0^{(2)}$ (the facets between creases 1 and 2, and 2 and 3, respectively), and then joining the facets with a copy of themselves reflected about the plane orthogonal to $\hat{\mathbf{e}}_2$. Let $\Omega_0^{(h)} := \Omega_0^{(1)} \cup \Omega_0^{(2)}$. Then $\Omega_0 = \text{Orb}_{\mathcal{G}} \Omega_0^{(h)}$ where $\mathcal{G} = \{\mathbf{I}, \sigma_{\hat{\mathbf{e}}_2}\}$ and $\text{Orb}_{\mathcal{H}} \square := \bigcup_{g \in \mathcal{H}} g(\square)$ is called the orbit of \square under the group \mathcal{H} . The implication here is that we can generate a folded configuration by folding $\Omega_0^{(h)}$ (i.e. $\Omega_0^{(h)} \rightarrow \Omega^{(h)}$) and then letting $\Omega = \text{Orb}_{\mathcal{G}} \Omega^{(h)}$. The caveat is that we require that $\hat{\mathbf{c}}_1 \cdot \hat{\mathbf{e}}_2 = \hat{\mathbf{c}}_3 \cdot \hat{\mathbf{e}}_2 = 0$ for there to be no tears, where $\hat{\mathbf{c}}_i$ is the unit vector along crease i in the deformed configuration. In other words, the orbit will be a compatible configuration provided that $\Omega^{(h)}$ and $\sigma_{\hat{\mathbf{e}}_2} \Omega^{(h)}$ overlap at creases 1 and 3. This represents a dimensional reduction of (6), which depends on ϕ_1, \dots, ϕ_4 , to the condition that $\hat{\mathbf{c}}_3 \cdot \hat{\mathbf{e}}_2 = 0$, which only depends on ϕ_1 and ϕ_2 . As alluded to previously, we recall that the

² Here, by “rigid rotation”, we mean that the entire origami is rotated such that all of the fold angles are preserved.

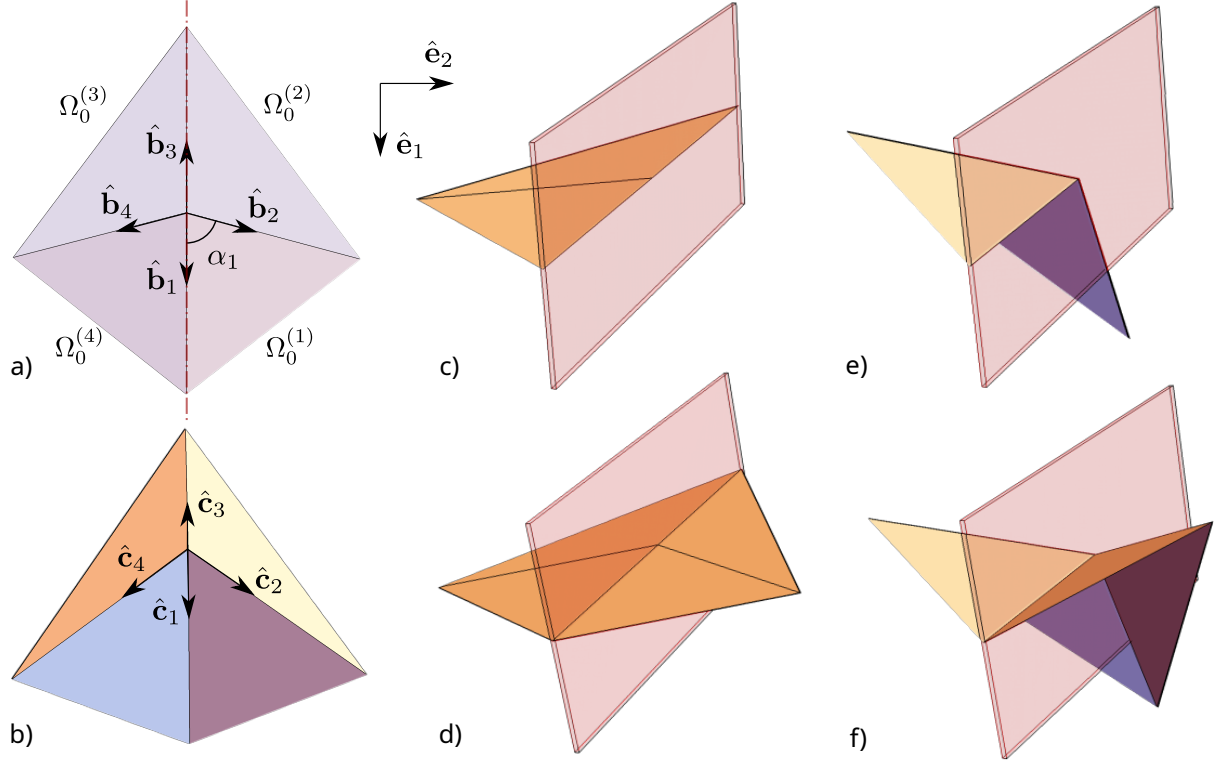


FIG. 1. **Geometry, coordinate system, and symmetric folding of the degree 4 vertex with reflection symmetry.** a) Geometry of the 4 vertex with a reflection symmetry and parameterized by the sector angle between the first two creases, α_1 . b) Folded configuration with crease vectors $\hat{\mathbf{c}}_i, i = 1, 2, 3, 4$ superimposed. c) Half of the flat configuration. d) Full flat configuration generated by the action $\sigma_{\hat{\mathbf{e}}_2} (\Omega_0^{(1)} \cup \Omega_0^{(2)})$. e) Half of the flat configuration folded such that $\hat{\mathbf{c}}_3$ is in the plane of symmetry, i.e. $\hat{\mathbf{c}}_3 \cdot \hat{\mathbf{e}}_2 = 0$. f) Full folded configuration generated by the action $\sigma_{\hat{\mathbf{e}}_2} (\Omega_0^{(1)} \cup \Omega_0^{(2)})$.

deformation map is only meaningful up to rigid rotations and translations of the entire body and so we first rotate $\Omega_0^{(1)}$ and $\Omega_0^{(2)}$ by $\mathbf{Q}_{\hat{\mathbf{b}}_1}(\phi_1/2)$. As a result, our deformation map has been adjusted such that

$$\mathbf{F}_1 = \mathbf{Q}_{\hat{\mathbf{b}}_1} \left(\frac{\phi_1}{2} \right), \quad \mathbf{F}_2 = \mathbf{Q}_{\hat{\mathbf{b}}_1} \left(\frac{\phi_1}{2} \right) \mathbf{Q}_{\hat{\mathbf{b}}_2}(\phi_2). \quad (8)$$

Given this adjusted but equivalent formulation, we now solve for ϕ_2 as a function of ϕ_1 such that

$$\hat{\mathbf{c}}_3 \cdot \hat{\mathbf{e}}_2 = \left(\mathbf{F}_2 \hat{\mathbf{b}}_3 \right) \cdot \hat{\mathbf{e}}_2 = \left(\mathbf{Q}_{\hat{\mathbf{b}}_1} \left(\frac{\phi_1}{2} \right) \mathbf{Q}_{\hat{\mathbf{b}}_2}(\phi_2) \hat{\mathbf{b}}_3 \right) \cdot \hat{\mathbf{e}}_2 = 0. \quad (9)$$

A schematic of this solution process is shown in fig. 1. The solution to (9) is readily obtained as

$$\phi_1 = 2 \arctan (\cos \alpha_1 \csc \phi_2 (\cos \phi_2 - 1)) \quad (10)$$

which agrees with solutions for 4 vertices published in the literature [38, 46, 66, 71]. From here we have that $\phi_4 = \phi_2$ (since $\hat{\mathbf{b}}_4 = \sigma_{\hat{\mathbf{e}}_2} \hat{\mathbf{b}}_2$) and it remains to compute ϕ_3 . In principle, we

could substitute ϕ_1, ϕ_2 , and ϕ_4 into (6) and solve for ϕ_3 . However, once again, the Lagrangian perspective lends itself towards the solution. We instead use what is currently known about the deformation map:

$$\begin{aligned}\mathbf{n}_2 &= \hat{\mathbf{c}}_2 \times \hat{\mathbf{c}}_3, \\ \phi_3 &= -\text{sgn}(\mathbf{n}_2 \cdot \hat{\mathbf{e}}_2) \arccos\left(\frac{\mathbf{n}_2 \cdot (\boldsymbol{\sigma}_{\hat{\mathbf{e}}_2} \mathbf{n}_2)}{\mathbf{n}_2 \cdot \mathbf{n}_2}\right).\end{aligned}\quad (11)$$

where \mathbf{n}_3 is a vector orthogonal to $\Omega^{(3)}$ ³.

IV. VERTICES WITH A REFLECTION SYMMETRY

While the previous section appealed to a geometric lens, here we explore the method through an algebraic lens, and its generalization to even number of creases, N . In general, for an origami which can be described by $\Omega_0 = \text{Orb}_{\mathcal{G}} \Omega_0^{(c)}$ for some unit cell $\Omega_0^{(c)}$ and group \mathcal{G} , we can rewrite (6) as

$$\prod_{i=1}^N \mathbf{Q}_{g_i \cdot \hat{\mathbf{b}}'_i}(\phi_i) = \mathbf{I} \quad (12)$$

where $g_i \cdot \hat{\mathbf{b}}'_i = \hat{\mathbf{b}}_i$ for some $g_i \in \mathcal{G}$ and $\hat{\mathbf{b}}'_i \in \Omega_0^{(c)}$ and where the index i is necessary because, in general, not all creases will be mapped from the same crease in $\Omega_0^{(c)}$ or under the same action transformation, g_i . The algebraic difficulty of (12) stems from the fact that 1) the rotations are taken about different axes and 2) the transformations do not commute. Thus, a potential strategy for simplifying (12) consists of reformulating in terms of like axes and taking advantage of transformations that commute in order to combine terms. Towards this end, we note the following useful identities

$$\mathbf{Q}_{\hat{\mathbf{u}}}^T(\varphi) = \mathbf{Q}_{\hat{\mathbf{u}}}(-\varphi) = \mathbf{Q}_{-\hat{\mathbf{u}}}(\varphi), \quad (13a)$$

$$\boldsymbol{\sigma}_{\hat{\mathbf{u}}} = \boldsymbol{\sigma}_{\hat{\mathbf{u}}}^T \quad (13b)$$

$$\mathbf{Q}_{\hat{\mathbf{u}}}(\varphi) \mathbf{Q}_{\hat{\mathbf{u}}}(\varphi') = \mathbf{Q}_{\hat{\mathbf{u}}}(\varphi + \varphi'), \quad (13c)$$

$$\mathbf{Q}_{\mathbf{O}\hat{\mathbf{u}}}(\varphi) = \mathbf{O} \mathbf{Q}_{\hat{\mathbf{u}}}(|\mathbf{O}|\varphi) \mathbf{O}^T, \quad \forall \mathbf{O} \in O(3), \quad (13d)$$

$$\mathbf{Q}_{\hat{\mathbf{u}}}(\varphi) = \mathbf{Q}_{\boldsymbol{\sigma}_{\hat{\mathbf{v}}}\hat{\mathbf{u}}}(\varphi) = \boldsymbol{\sigma}_{\hat{\mathbf{v}}}\mathbf{Q}_{\hat{\mathbf{u}}}(-\varphi)\boldsymbol{\sigma}_{\hat{\mathbf{v}}}, \quad \forall \hat{\mathbf{u}}, \hat{\mathbf{v}} \text{ such that } \hat{\mathbf{u}} \cdot \hat{\mathbf{v}} = 0. \quad (13e)$$

$$\boldsymbol{\sigma}_{\hat{\mathbf{u}}}\boldsymbol{\sigma}_{\hat{\mathbf{v}}} = \mathbf{Q}_{\hat{\mathbf{w}}}(2 \arccos(\hat{\mathbf{u}} \cdot \hat{\mathbf{v}})), \quad \hat{\mathbf{w}} := \frac{\hat{\mathbf{u}} \times \hat{\mathbf{v}}}{|\hat{\mathbf{u}} \times \hat{\mathbf{v}}|} \quad (13f)$$

$$\boldsymbol{\sigma}_{\hat{\mathbf{u}}}\boldsymbol{\sigma}_{\hat{\mathbf{v}}} = \boldsymbol{\sigma}_{\hat{\mathbf{v}}}\boldsymbol{\sigma}_{\hat{\mathbf{u}}}, \quad \forall \hat{\mathbf{u}}, \hat{\mathbf{v}} \text{ such that } \hat{\mathbf{u}} \cdot \hat{\mathbf{v}} = 0, \quad (13g)$$

$$\boldsymbol{\sigma}_{\hat{\mathbf{u}}}\mathbf{Q}_{\hat{\mathbf{u}}}(\varphi) = \mathbf{Q}_{\hat{\mathbf{u}}}(\varphi)\boldsymbol{\sigma}_{\hat{\mathbf{u}}}. \quad (13h)$$

Consider a vertex with crease unit vectors

$$\hat{\mathbf{b}}_1, \dots, \hat{\mathbf{b}}_{N/2}, \quad \hat{\mathbf{b}}_{N/2+1} = -\hat{\mathbf{b}}_1, \quad \hat{\mathbf{b}}_{N/2+2} = \boldsymbol{\sigma}_{\hat{\mathbf{e}}_2} \hat{\mathbf{b}}_{N/2}, \quad \dots, \quad \hat{\mathbf{b}}_N = \boldsymbol{\sigma}_{\hat{\mathbf{e}}_2} \hat{\mathbf{b}}_2. \quad (14)$$

such that the vertex has a reflection symmetry in the flat, reference configuration. The coordinate system is chosen as Euclidean such that $\hat{\mathbf{e}}_3$ is orthogonal to the flat configuration

³ A simplified solution to (11) is given in appendix A.

and the reflection symmetry is about the plane orthogonal to $\hat{\mathbf{e}}_2$. Let $\mathcal{G} = \{\mathbf{I}, \sigma_{\hat{\mathbf{e}}_2}\}$. Then (12) takes the form of

$$\mathbf{Q}_{\hat{\mathbf{b}}_1}(\phi_1) \cdots \mathbf{Q}_{\hat{\mathbf{b}}_{N/2}}(\phi_{N/2}) \mathbf{Q}_{-\hat{\mathbf{b}}_1}(\phi_{N/2+1}) \mathbf{Q}_{\sigma_{\hat{\mathbf{e}}_2} \hat{\mathbf{b}}_{N/2}}(\phi_{N/2+2}) \cdots \mathbf{Q}_{\sigma_{\hat{\mathbf{e}}_2} \hat{\mathbf{b}}_2}(\phi_N) = \mathbf{I}, \quad (15)$$

which by (13) is equivalent to

$$\begin{aligned} & \mathbf{Q}_{\hat{\mathbf{b}}_1} \left(\frac{\phi_1}{2} \right) \cdots \mathbf{Q}_{\hat{\mathbf{b}}_{N/2}}(\phi_{N/2}) \mathbf{Q}_{\hat{\mathbf{b}}_1}(-\phi_{N/2+1}) \times \\ & \sigma_{\hat{\mathbf{e}}_2} \mathbf{Q}_{\hat{\mathbf{b}}_{N/2}}(-\phi_{N/2+1}) \cdots \mathbf{Q}_{\hat{\mathbf{b}}_2}(-\phi_N) \mathbf{Q}_{\hat{\mathbf{b}}_1} \left(-\frac{\phi_1}{2} \right) \sigma_{\hat{\mathbf{e}}_2} = \mathbf{I}. \end{aligned} \quad (16)$$

Similar to (A3a), we find that

$$\mathbf{Q}_{\hat{\mathbf{b}}_1} \left(\frac{\phi_1}{2} \right) \cdots \mathbf{Q}_{\hat{\mathbf{b}}_{N/2}}(\phi_{N/2}) \mathbf{Q}_{\hat{\mathbf{b}}_1}(-\phi_{N/2+1}) = \sigma_{\hat{\mathbf{e}}_2} \mathbf{Q}_{\hat{\mathbf{b}}_1} \left(\frac{\phi_1}{2} \right) \cdots \mathbf{Q}_{\hat{\mathbf{b}}_{N/2}}(\phi_{N/2}) \sigma_{\hat{\mathbf{e}}_2}, \quad (17)$$

represents a reduced-order formulation for solutions of (12) which have a symmetry described by \mathcal{G} . This can be reformulated as

$$\left(\mathbf{Q}_{\hat{\mathbf{b}}_1}(\phi_1/2) \mathbf{Q}_{\hat{\mathbf{b}}_2}(\phi_2) \cdots \mathbf{Q}_{\hat{\mathbf{b}}_{N/2}}(\phi_{N/2}) \hat{\mathbf{b}}_{N/2+1} \right) \cdot \hat{\mathbf{e}}_2 = 0. \quad (18)$$

Upon satisfying (18), and plugging into (16), one readily sees that

$$\phi_{N/2+2} = \phi_{N/2}, \quad \phi_{N/2+3} = \phi_{N/2-1}, \quad \dots, \quad \phi_N = \phi_2 \quad (19)$$

is a solution. An example of the algebraic approach applied to degree 4 vertices with reflection symmetry is given in appendix A. While the primary focus of this work is on closed-form solutions, a reduced order computational approach, based on (18) and seminal work by Tachi [48], is also outlined in the supplementary information.

We will next obtain multi-degree of freedom, closed-form solutions to (18) for degree 6 and degree 8 vertices. In general, equation (18) is still difficult to solve because it is nonlinear and contains the unknowns as arguments of trigonometric functions. However, in comparison to (6), there multiple simplifications worth noting. The first, which has already been mentioned, is that the number of unknowns has been reduced—specifically, the number of degrees of freedom is reduced from $N - 3$ to $N/2 - 1$. The second simplification is also important: *while (6) represents a system of 3 simultaneous, nonlinear equations, (42) is only a single nonlinear equation instead of a system.* Throughout this work, kinematic solutions are found and simplified using the powerful symbolic computation algorithms in Mathematica [75]. Although simultaneous nonlinear equations can be prohibitively difficult to solve, Mathematica has powerful algorithms for using a wide array of trigonometric identities to solve and simplify realizations of (42).

A. 6-vertex

In this section, we consider 6 vertices with a reflection symmetry parameterized by α_1 such that $\alpha_3 = \alpha_1$ and $\alpha_2 = \pi - 2\alpha_1$, as shown in fig. 2. The reduced order compatibility

condition (17) for this system admits a closed-form solution:

$$\begin{aligned}
\phi_1 &= f_\phi(2 \arctan(-\mathcal{S}_6 \mathcal{Y}_6, \mathcal{S}_6 \mathcal{X}_6)), \\
\mathcal{Y}_6 &= \cos \alpha_1 \sin \alpha_1 \left(2 \cos^2 \alpha_1 \sin^2 \frac{\phi_3}{2} (1 - 2 \cos \phi_2) - \sin^2 \alpha_1 + \right. \\
&\quad \left. \cos \phi_3 (1 - \cos \phi_2 + \sin^2 \alpha_1) + \sin \phi_2 \sin \phi_3 \right), \\
\mathcal{X}_6 &= \sin \alpha_1 \left(\sin \phi_2 + 2 \cos(2\alpha_1) \sin \phi_2 \sin^2 \frac{\phi_3}{2} + \cos \phi_2 \sin \phi_3 \right), \\
\mathcal{S}_6 &= \pm 1,
\end{aligned} \tag{20}$$

where $\arctan(y, x)$ considers the quadrant in which (x, y) resides, and where \mathcal{S}_6 helps specify the quadrant of $(\mathcal{X}_6, \mathcal{Y}_6)$. Of these two possible solutions, only one satisfies compatibility for a general ϕ_2, ϕ_3 , and α_1 . While it is difficult to determine analytically which solution is valid, we speculate that

$$\mathcal{S}_6 = \operatorname{sgn} \left(\cos \phi_2 \sin \phi_3 + 2 \cos(2\alpha_1) \sin \phi_2 \sin^2 \frac{\phi_3}{2} + \sin \phi_2 \right) \tag{21}$$

is correct, and suggest relying on numerical verification in practice. Lastly,

$$f_\phi(\varphi) = \begin{cases} f_\phi(\varphi + 2\pi) & \varphi < -\pi \\ f_\phi(\varphi - 2\pi) & \varphi > \pi \\ \varphi & \text{otherwise} \end{cases}, \tag{22}$$

converts fold angles into the allowable range prior to contact of adjacent faces (i.e. $[-\pi, \pi]$). The solution was found and simplified using the powerful symbolic computation algorithms in Mathematica [75]. The Mathematica notebook can be found here. It was then verified by numerically evaluating $\|\prod_{i=1}^6 \mathbf{Q}_{\mathbf{b}_i}(\phi_i) - \mathbf{I}\|_2$ and finding that it was $\lesssim 10^{-16}$ throughout the domain, $(\phi_2, \phi_3) \in [-\pi, \pi] \times [-\pi, \pi]$.

Folded states of the 6-vertex with $\alpha_1 = \pi/6$ for various combinations of $\phi_2 \in \{-\pi/4, 0, \pi/4\}$ and $\phi_3 \in \{-\pi/4, 0, \pi/4\}$ are shown in fig. 3.a; and contours of ϕ_1 as a function of ϕ_2 and ϕ_3 are shown in fig. 3.b. Regions of (ϕ_2, ϕ_3) space which are inadmissible due to self-contact are shown in white. The procedure for detecting self-contact is outlined in appendix B. An animation of the highlighted folding trajectory is provided in the ESI (see Animation #1). When self contact occurs in any of the folding animations, the frame is tinted red to signal the configuration is inadmissible.

The top row of kinematic contour plots in fig. 3.b corresponds with vertices where the folds can be divided into two groups of creases which are “near” to each other (e.g. when $\alpha_1 = \pi/12$ (top-left), creases 1, 2, and 6 are all within $\pi/6$ of each other and similarly, creases 3, 4, and 5 are all within $\pi/6$ of each other). The way that crease 1 folds as a function of ϕ_2 and ϕ_3 is similar in character for each of these two cases. In contrast, the bottom row of fig. 3.b shows that, $\phi_1 = \phi_1(\phi_2, \phi_3)$ is characteristically different when increasing α_1 such that creases 2 and 3 are closer together. The kinematic contours for $\alpha_1 = \pi/3$ and $5\pi/12$ are similar, but the $\alpha_1 = 5\pi/12$ contours for moderate $|\phi_1|$ have expanded relative to

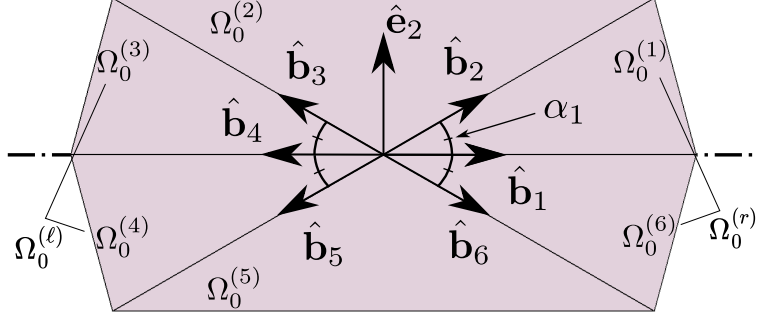


FIG. 2. **Geometry, coordinate system, and symmetry of the degree 6 vertex with reflection symmetry.** a) Geometry of the 6 vertex with a reflection symmetry. The vertex is parameterized by the sector angle between the first two creases, α_1 . b) Coordinate system, axis of symmetry, and facet labels, $\Omega_0^{(i)}$, $i = 1, \dots, 6$. We define $\Omega_0^{(r)} := \Omega_0^{(1)} \cup \Omega_0^{(6)}$ and $\Omega_0^{(\ell)} := \Omega_0^{(3)} \cup \Omega_0^{(4)}$.

their $\alpha_1 = \pi/3$ counterparts; vice versa, the contours for greater magnitude fold angles (i.e. $|\phi_1| > \pi/2$) have contracted relative to their analog in the $\alpha_1 = \pi/3$ case. Crease 1 folds less, in general, as a function of ϕ_2 and ϕ_3 , for increasing α_1 (when $\alpha_1 \geq \pi/3$). This phenomena is illustrated in fig. 4.a where various folded states of a 6-vertex with $\alpha_1 = 11\pi/24$ are shown. Let $\Omega^{(r)} := \Omega^{(1)} \cup \Omega^{(6)}$ and $\Omega^{(\ell)} := \Omega^{(3)} \cup \Omega^{(4)}$ (see fig. 2). As $\alpha_1 \rightarrow \pi/2$, creases 2, 3, 5 and 6 act collectively as a kind of hinge such that $\Omega^{(r)}$ and $\Omega^{(\ell)}$ can fold toward or away from each other without much flexing across their middle creases. The change in geometry and kinematics as a function of α_1 has important implications for self-contact as well. The number of holes in admissible space, the size of the admissible regions, and the connectivity between admissible regions changes with α_1 . For instance, the bottom-left and top-right admissible regions only connect at a single point, the flat configuration (i.e. $(0,0)$), for the $\alpha_1 = \pi/6$ and $\pi/4$ cases, but at 3 points for the $\alpha = 5\pi/12$ case. To help illustrate why, animations of the $\alpha_1 = \pi/4$ and $\alpha_1 = 5\pi/12$ vertices folding along ($\phi_2 = 0 \rightarrow -\pi, \phi_3 = \pi$) and then ($\phi_2 = -\pi, \phi_3 = \pi \rightarrow 0$) are provided in the ESI as Animation #2 and Animation #3, respectively. When α_1 is small, facets $\Omega_0^{(2)}$ and $\Omega_0^{(5)}$ are “large” and appear to contact each other through nearly the entire folding motion of the $\alpha_1 = \pi/4$ vertex. Whereas $\Omega_0^{(2)}$ and $\Omega_0^{(5)}$ are much smaller when $\alpha_1 = 5\pi/12$, so that the two flaps on either end of the vertex are able to nest within each other during the folding.

By construction, $\phi_5 = \phi_3$ and $\phi_6 = \phi_2$. Having obtained $\phi_1 = \phi_1(\phi_2, \phi_3)$ (equation (20)), what remains of the kinematic description of the 6-fold vertex is ϕ_4 . Similar to section III, we derive the remaining fold angle by appealing to the deformation map and noting that

$$\begin{aligned}\hat{\mathbf{c}}_3 &= \mathbf{F}_2 \hat{\mathbf{b}}_3 = \mathbf{Q}_{\hat{\mathbf{b}}_1}(\phi_1/2) \mathbf{Q}_{\hat{\mathbf{b}}_2}(\phi_2) \hat{\mathbf{b}}_3, \\ \hat{\mathbf{c}}_4 &= \mathbf{F}_3 \hat{\mathbf{b}}_4 = \mathbf{Q}_{\hat{\mathbf{b}}_1}(\phi_1/2) \mathbf{Q}_{\hat{\mathbf{b}}_2}(\phi_2) \mathbf{Q}_{\hat{\mathbf{b}}_3}(\phi_3) \hat{\mathbf{b}}_4.\end{aligned}\tag{23}$$

Given these crease vectors, the following yields normal vectors to $\Omega^{(3)}$ and $\Omega^{(4)}$, and eventually ϕ_4 :

$$\begin{aligned}\mathbf{n}_3 &= \hat{\mathbf{c}}_3 \times \hat{\mathbf{c}}_4, \\ \phi_4 &= -\text{sgn}(\mathbf{n}_3 \cdot \hat{\mathbf{e}}_2) \arccos\left(\frac{\mathbf{n}_3 \cdot (\boldsymbol{\sigma}_{\hat{\mathbf{e}}_2} \mathbf{n}_3)}{\mathbf{n}_3 \cdot \mathbf{n}_3}\right).\end{aligned}\tag{24}$$

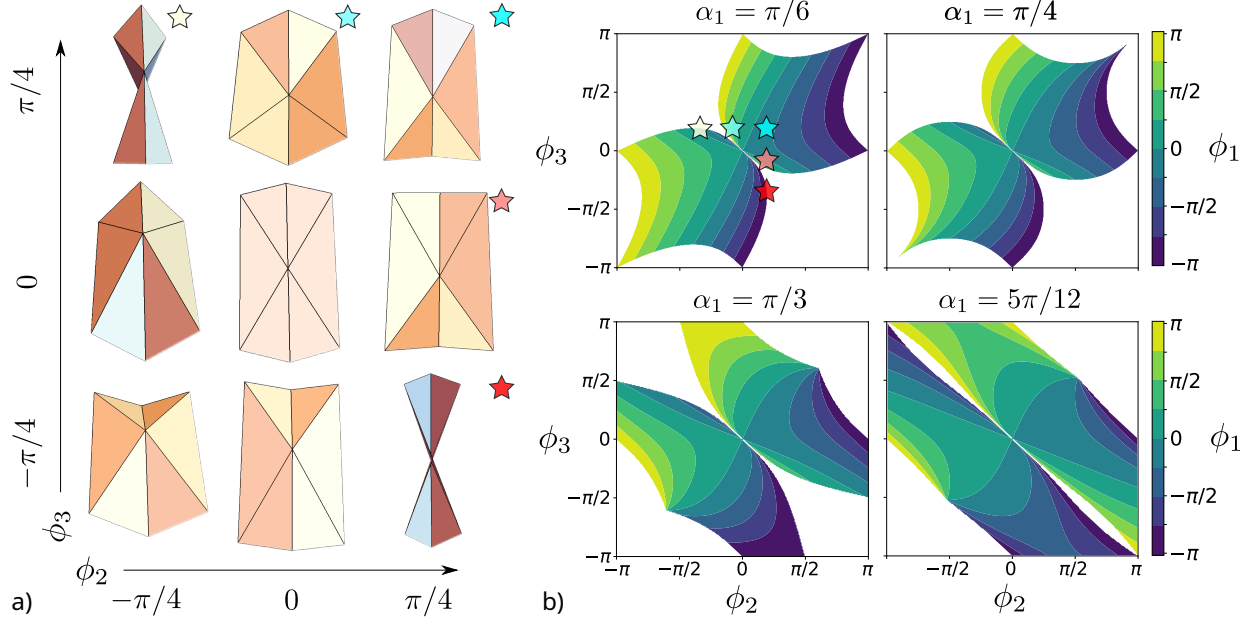


FIG. 3. **Degrees of freedom and kinematics of the degree 6 vertex with reflection symmetry.** a) Folded states of a 6-vertex with a reflection symmetry and with $\alpha_1 = \pi/6$ and $\alpha_2 = \pi - 2\alpha_1$. Traversing columns (i.e. right-to-left) corresponds with changing ϕ_2 and traversing rows (i.e. bottom-to-top) corresponds with changing ϕ_3 . b) Contours of ϕ_1 as a function of ϕ_2 (x-axis) and ϕ_3 (y-axis) for $\alpha_1 = \pi/6, \pi/4, \pi/3$, and $5\pi/12$ (top-left, top-right, bottom-left, and bottom-right, respectively). White regions are inadmissible due to contact; note that the number of holes in admissible space, the size of the admissible regions, and the connectivity between admissible regions changes with α_1 .

An explicit (albeit complicated) expression for \mathbf{n}_3 is given by

$$\begin{aligned}
 \mathbf{n}_3 = \sin \phi_1 \cos \phi_3 \left\{ \right. & \left[\sin \phi_1 \left(\sin \phi_2 + \tan \phi_3 \left(2 \cos^2 \alpha_1 - \cos(2\alpha_1) \cos \phi_2 \right) \right) \right] \hat{\mathbf{e}}_1 \\
 & + \left[\frac{\cos \phi_2}{2} \left(\cos \alpha_1 \cos \frac{\phi_1}{2} \tan \phi_3 - 2 \sin \frac{\phi_1}{2} \right) - \cos 2\alpha_1 \sin \frac{\phi_1}{2} \sin \phi_2 \tan \phi_3 \right. \\
 & \quad \left. - \cos \alpha_1 \cos \frac{\phi_1}{2} \left(\sin \phi_2 - 2 \sin^2 \alpha_1 \tan \phi_3 \right) \right] \hat{\mathbf{e}}_2 \\
 & + \left[\cos \frac{\phi_1}{2} \left(\cos \phi_2 + \cos \alpha_1 \sin \phi_2 \tan \phi_3 \right) \right. \\
 & \quad \left. + \frac{\sin \phi_2 / 2}{2} \left(\tan \phi_3 \left(\cos \alpha_1 \cos \phi_2 + 4 \cos \alpha_1 \sin^2 \alpha_1 \right) - 2 \cos \alpha_1 \sin \phi_2 \right) \right] \hat{\mathbf{e}}_3 \left. \right\}.
 \end{aligned} \tag{25}$$

The contours of $\phi_4 = \phi_4(\phi_2, \phi_3)$ are shown in fig. 4.b. Again, as before with $\phi_1 = \phi_1(\phi_2, \phi_3)$ (fig. 3.b), we see that 1) the cases where $\alpha_1 < \pi/3$ (top row) are characteristically different than the cases where $\alpha_1 \geq \pi/3$ (bottom row) and 2) for the case of $\alpha_1 = 5\pi/12$ (bottom-

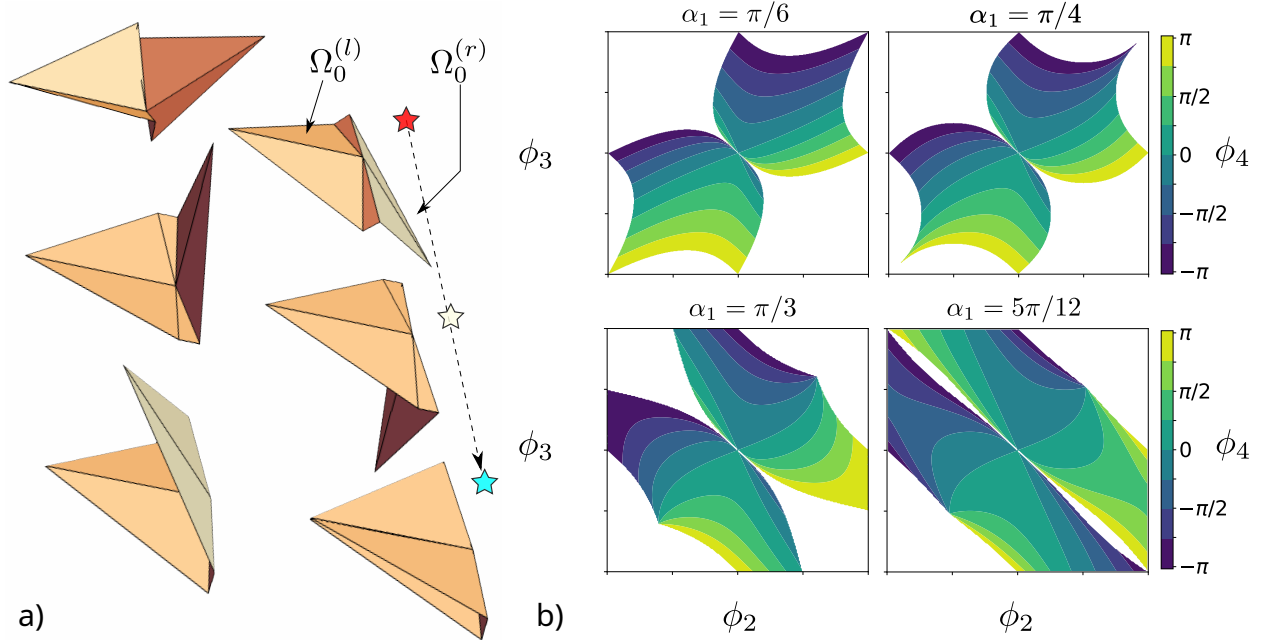


FIG. 4. **Dependence of 6 vertex kinematics on α_1 and hinge-like behavior.** a) Folded states of a 6-vertex with a reflection symmetry and with $\alpha_1 = 11\pi/24$ and $\alpha_2 = \pi - 2\alpha_1$. As $\alpha_1 \rightarrow \pi/2$, creases 2, 3, 5 and 6 act collectively as a kind of hinge such that $\Omega^{(r)}$ and $\Omega^{(l)}$ can fold toward or away from each other without a lot of folding across their middle creases (crease 1 and 4, respectively). b) Contours of ϕ_4 as a function of ϕ_2 (x-axis) and ϕ_3 (y-axis) for $\alpha_1 = \pi/6, \pi/4, \pi/3$, and $5\pi/12$ (top-left, top-right, bottom-left, and bottom-right, respectively).

right), creases 2, 3, 5, and 6 behave collectively as a kind of hinge that requires minimal folding at crease 4 for a significant range its of motion. Interestingly, in comparing the bottom-right panels of fig. 3.b and fig. 4.b, which show, for the case of $\alpha_1 = 5\pi/12$, the contours of ϕ_1 and ϕ_4 , respectively, we see that $\phi_4 = \phi_1$ for nearly the whole domain. It is as if, in the limit of $\alpha_1 \rightarrow \pi/2$ where creases 2 and 3 collapse onto each other, a property of the symmetric 4-vertex is recovered: its two creases within the plane of symmetry have equal and opposite fold angle. To highlight this, snapshots of folded configurations of an $\alpha_1 = 11\pi/24$ vertex are shown in fig. 4.a, and an animation of the folded trajectory marked by stars is provided in the ESI (see Animation #4).

Before moving on, we note an important symmetry inherent in the solutions for the fold angles obtained thus far. Consider taking a folded origami and flipping it upside-down; then all of the valley folds appear mountain and all of the mountain folds appear valley. In other words, classifying the folds as mountain or valley implies a choice of \hat{e}_3 . Thus, there is a symmetry associated with simultaneously making the transformations: $\hat{e}_3 \rightarrow -\hat{e}_3$ and “valley” \leftrightarrow “mountain” (and, consequently, $\phi_i \rightarrow -\phi_i, i = 1, \dots, N$). We should expect an invariance with respect to this in general. We give it the name *flip invariance*. Upon close inspection of (20), one can see that it is indeed flip invariant. However, flip invariance is also readily illustrated in the contours of $\phi_1 = \phi_1(\phi_2, \phi_3)$ (fig. 3) and $\phi_4 = \phi_4(\phi_2, \phi_3)$ (fig. 4). Take any point in the (ϕ_2, ϕ_3) domain and invert it about the origin, $(\phi_2, \phi_3) \rightarrow (-\phi_2, -\phi_3)$. The contour you arrive at is of the same magnitude, but opposite sign, as expected.

B. 8-vertex

Next we consider the crease pattern for a classical origami base: the symmetric 8-fold waterbomb. The solution for its fully symmetric, single-degree of freedom folding with alternating mountain and valley creases is well known [29, 67, 68]. This, however, represents a 1-dimensional trajectory through its 5-dimensional configuration space. Here we use the reflection symmetry to dimensionally reduce the problem to 3 degrees of freedoms; then solve, simplify, and verify using a computer algebra system. This allows us to explore a higher dimensional submanifold than in past work.

For a given (ϕ_2, ϕ_3, ϕ_4) , an explicit 3 degree of freedom solution is given by one of the four solutions⁴

$$\phi_1 = \begin{cases} f_\phi (2 \arctan (\mathcal{S}_8 (\mathcal{A}_8 + \mathcal{B}_8), \mathcal{S}_8 \mathcal{C}_8)) \\ f_\phi (2 \arctan (\mathcal{S}_8 \mathcal{C}_8), \mathcal{S}_8 (\mathcal{A}_8 - \mathcal{B}_8)) \end{cases}, \quad (26a)$$

where $\mathcal{S}_8 = \pm 1$, and where

$$\begin{aligned} \mathcal{A}_8 (\phi_2, \phi_3, \phi_4) &:= 4 \cos \left(\phi_2 + \frac{\phi_4}{2} \right) \cos \frac{\phi_4}{2} \sin \phi_3, \\ \mathcal{B}_8 (\phi_2, \phi_3, \phi_4) &:= \sqrt{2} (\sin \phi_2 (1 + \cos \phi_3 + (\cos \phi_3 - 1) \cos \phi_4) + 2 \cos \phi_2 \cos \phi_3 \sin \phi_4), \\ \mathcal{C}_8 (\phi_2, \phi_3, \phi_4) &:= 1 - \cos \phi_4 - \sqrt{2} \sin \phi_2 \sin \phi_3 (1 + \cos \phi_4) + \sqrt{2} \sin \phi_3 \sin \phi_4 - \\ &\quad \cos \phi_3 (1 + \cos \phi_4 + 2 \sin \phi_2 \sin \phi_4) + \\ &\quad \cos \phi_2 \left(1 + \cos \phi_3 + \cos \phi_4 (\cos \phi_3 - 1) - \sqrt{2} \sin \phi_3 \sin \phi_4 \right). \end{aligned} \quad (26b)$$

The minimum numerical error was tested extensively and found, that in every case considered, the error was within numerical precision (i.e. $\|\prod_{i=1}^8 \mathbf{Q}_{\hat{\mathbf{b}}_i}(\phi_i) - \mathbf{I}\|_2 \lesssim 10^{-16}$). Given ϕ_1, \dots, ϕ_4 , the fold angle ϕ_5 was computed by

$$\begin{aligned} \mathbf{n}_4 &= \hat{\mathbf{c}}_4 \times \hat{\mathbf{c}}_5, \\ \phi_5 &= -\text{sgn}(\mathbf{n}_4 \cdot \hat{\mathbf{e}}_2) \arccos \left(\frac{\mathbf{n}_4 \cdot (\boldsymbol{\sigma}_{\hat{\mathbf{e}}_2} \mathbf{n}_4)}{\mathbf{n}_4 \cdot \mathbf{n}_4} \right). \end{aligned} \quad (27)$$

Contours of slices of $\phi_1 = \phi_1(\phi_2, \phi_3, \phi_4)$ (top-row) and $\phi_5 = \phi_5(\phi_2, \phi_3, \phi_4)$ (bottom-row) are shown in fig. 5 for fixed $\phi_4 = -\pi/2, -\pi/4, \pi/4, \text{ and } \pi/2$ (left column), and fixed $\phi_3 = -\pi/2, -\pi/4, \pi/4, \text{ and } \pi/2$ (right column). The information rich equation (26) and fig. 5 show a reduced picture of the many different possible ways of folding, and associated degrees of freedom, for the symmetric 8-fold waterbomb vertex; however, the expressions are complex. In the next section, we extend the approach to allow for further reduction of dimensionality and exploitation of symmetry.

⁴ Analytic determination of which of the four solutions is valid for some (ϕ_2, ϕ_3, ϕ_4) is difficult, in general. However, when working numerically, it is trivial to plug ϕ_1, \dots, ϕ_8 into (6) for each of the four solutions and check which results in the least error.

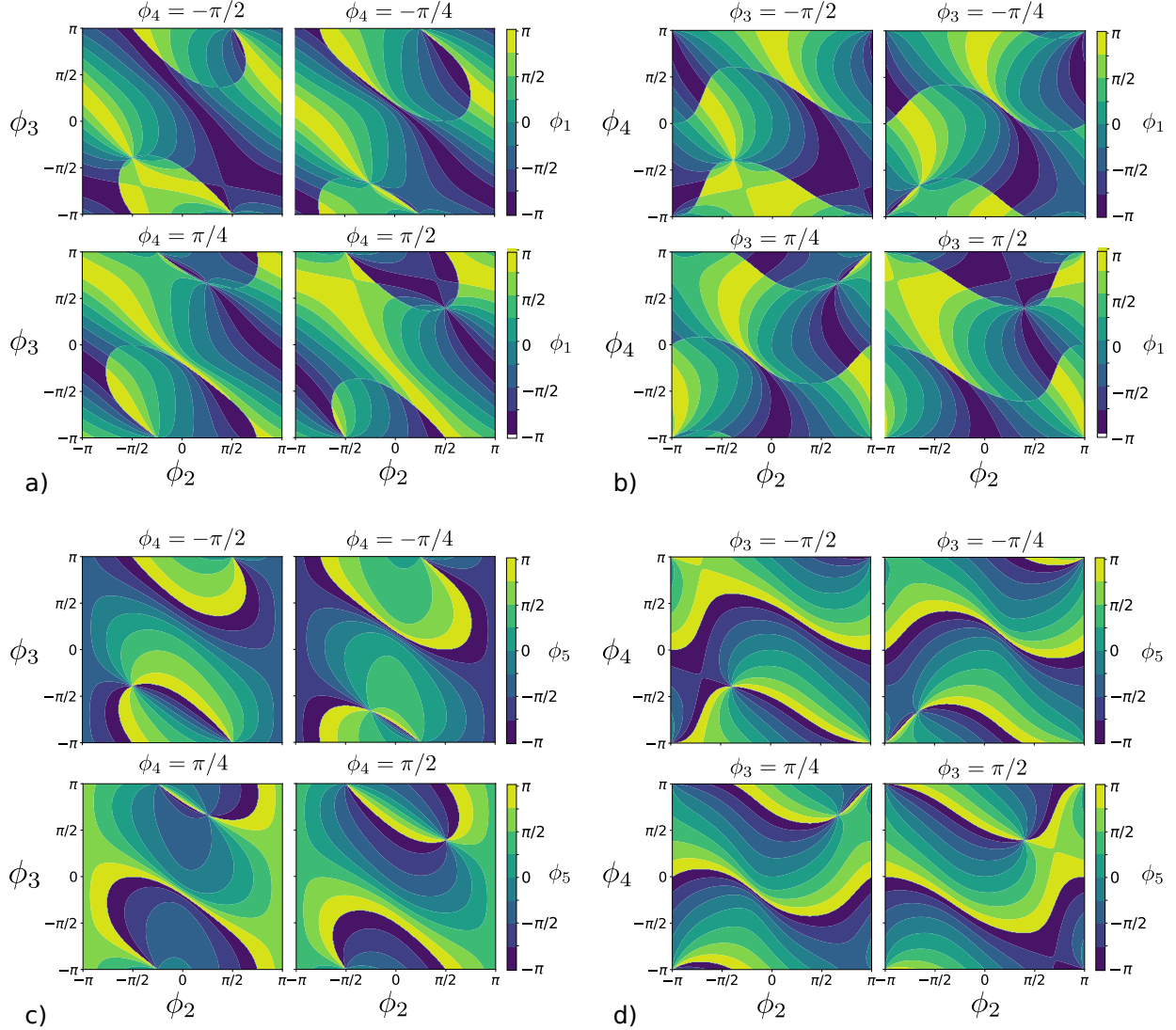


FIG. 5. **Kinematics of the degree 8 vertex with reflection symmetry.** Kinematics of a uniform 8-vertex such that the deformed vertices exhibit a reflection symmetry. Contours of slices of $\phi_1 = \phi_1(\phi_2, \phi_3, \phi_4)$ (top-row) and $\phi_5 = \phi_5(\phi_2, \phi_3, \phi_4)$ (bottom-row) are shown for fixed $\phi_4 = -\pi/2, -\pi/4, \pi/4,$ and $\pi/2$ (left column), and fixed $\phi_3 = -\pi/2, -\pi/4, \pi/4,$ and $\pi/2$ (right column). Note: self-contact not enforced in this visualization.

V. VERTICES WITH COMBINED ROTATIONS AND REFLECTIONS

A. 8-vertex

Next we adjust our choice (up to rigid body rotations) of the deformation map in order to exploit symmetry groups which also include rotations. Inspired by the kinematic parameterization of the fully symmetric folding for the 8-fold waterbomb used in Hanna et al. [67],

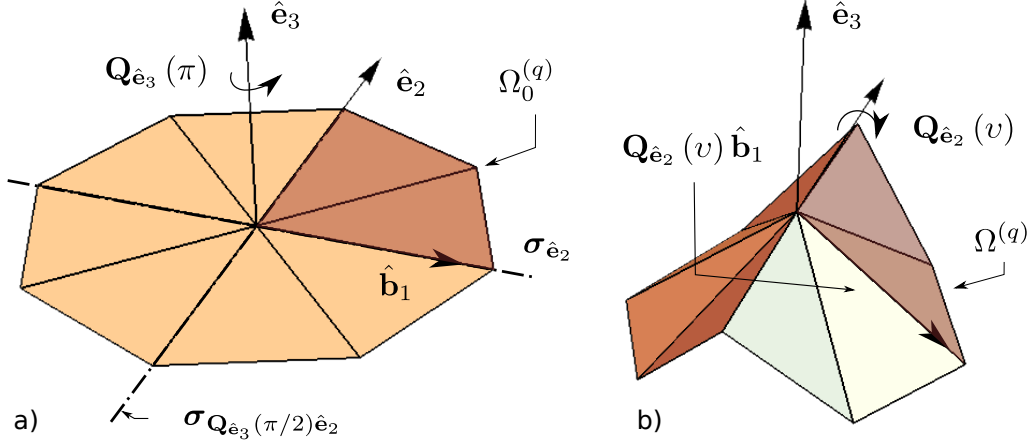


FIG. 6. **Deformation map for vertices with reflection and rotational symmetries.** a) The flat, reference configuration of a uniform degree 8 vertex can be described by $\text{Orb}_{\mathcal{G}} \Omega_0^{(q)}$ where $\Omega_0^{(q)} = \Omega_0^{(1)} \cup \Omega_0^{(2)}$ and $\mathcal{G} = \langle \sigma_{\hat{e}_2}, \mathbf{Q}_{\hat{e}_3}(\pi) \rangle$. b) The deformation map is chosen, up to rigid body rotations, such that $\Omega_0^{(q)}$ is first rotated by some angle of elevation ν and then folded; the modified parameterization of folded states allows the symmetry of the folded state to also be described by \mathcal{G} as \hat{e}_3 can then remain the axis of the rotational symmetry.

we consider first elevating crease 1 by rotating via $\mathbf{Q}_{\hat{e}_2}(\nu)^5$ and then deforming in the usual way, i.e.

$$\mathbf{F}_i = \begin{cases} \mathbf{Q}_{\hat{e}_2}(\nu) \mathbf{Q}_{\hat{b}_1}(\rho_1), & i = 1, \\ \mathbf{Q}_{\hat{e}_2}(\nu) \mathbf{Q}_{\hat{b}_1}(\rho_1) \prod_{j=2}^i \mathbf{Q}_{\hat{b}_j}(\phi_j), & i \neq 1 \end{cases} \quad (28)$$

where we introduce notation ρ_1 to denote the right *partial fold angle* at crease 1 (i.e. the contribution to the fold angle on the $+\hat{e}_2$ side of the crease). Previously, it was the case that $\rho_1 = \phi_1/2$, but for vertices with rotational symmetry this relationship can be relaxed and compatible states with less symmetry (such that the left and right partial fold angles are not necessarily equal) can be generated.

The parameterization introduced in (28) allows us to describe the symmetry of the folded state using the same symmetry group as the flat state. Indeed, let $\mathcal{G} = \langle \sigma_{\hat{e}_2}, \mathbf{Q}_{\hat{e}_3}(\pi) \rangle$ where $\langle \square \rangle$ is the group generated by \square ; and let $\Omega_0^{(q)} = \Omega_0^{(1)} \cup \Omega_0^{(2)}$. Then fig. 6.a shows that the flat state of the 8-fold waterbomb satisfies the symmetry described by \mathcal{G} ; and fig. 6.b shows an example folded configuration whose deformation is described by (28) and also satisfies the symmetry described by \mathcal{G} .

Geometrically, the significance of this reparameterization for the deformation map consists in its ability to use the orbit of the same group to construct the folded configuration from $\Omega^{(q)}$ as the group used to construct the flat configuration from $\Omega_0^{(q)}$. For the purposes of generalization, we now explore this reparameterization in its algebraic context. Note that, by (13f) and (13g), $\mathbf{Q}_{\hat{e}_3}(\pi) = \sigma_{\hat{e}_2} \sigma_{\hat{e}_1} = \sigma_{\hat{e}_1} \sigma_{\hat{e}_2}$. Assume for now that $\rho_1 = \phi_2/2$. Beginning

⁵ In [29, 67, 68], the analogous parameter is the angle, θ , between the vertical axis (i.e. unit direction orthogonal to the flat state) and the crease vector for the valley creases.

with (6):

$$\begin{aligned} & \mathbf{Q}_{\hat{\mathbf{e}}_2}(v) \mathbf{Q}_{\hat{\mathbf{b}}_1}(\rho_1) \mathbf{Q}_{\hat{\mathbf{b}}_2}(\phi_2) \mathbf{Q}_{\hat{\mathbf{b}}_3}(\phi_3) \mathbf{Q}_{\sigma_{\hat{\mathbf{e}}_1} \hat{\mathbf{b}}_2}(\phi_4) \mathbf{Q}_{\sigma_{\hat{\mathbf{e}}_1} \hat{\mathbf{b}}_1}(\phi_5) \times \\ & \mathbf{Q}_{\mathbf{Q}_{\hat{\mathbf{e}}_3}(\pi) \hat{\mathbf{b}}_2}(\phi_6) \mathbf{Q}_{\sigma_{\hat{\mathbf{e}}_2} \hat{\mathbf{b}}_3}(\phi_7) \mathbf{Q}_{\sigma_{\hat{\mathbf{e}}_2} \hat{\mathbf{b}}_2}(\phi_8) \mathbf{Q}_{\sigma_{\hat{\mathbf{e}}_2} \hat{\mathbf{b}}_1}(\rho_1) \mathbf{Q}_{\hat{\mathbf{e}}_2}(-v) = \mathbf{I}. \end{aligned} \quad (29)$$

Then by (13)

$$\begin{aligned} & \mathbf{Q}_{\hat{\mathbf{e}}_2}(v) \mathbf{Q}_{\hat{\mathbf{b}}_1}(\rho_1) \mathbf{Q}_{\hat{\mathbf{b}}_2}(\phi_2) \mathbf{Q}_{\hat{\mathbf{b}}_3}(\phi_3) \sigma_{\hat{\mathbf{e}}_1} \mathbf{Q}_{\hat{\mathbf{b}}_2}(-\phi_4) \mathbf{Q}_{\hat{\mathbf{b}}_1}(-\phi_5) \times \\ & \sigma_{\hat{\mathbf{e}}_2} \mathbf{Q}_{\hat{\mathbf{b}}_2}(\phi_6) \sigma_{\hat{\mathbf{e}}_1} \mathbf{Q}_{\hat{\mathbf{b}}_3}(-\phi_7) \mathbf{Q}_{\hat{\mathbf{b}}_2}(-\phi_8) \mathbf{Q}_{\hat{\mathbf{b}}_1}(\rho_1) \mathbf{Q}_{\hat{\mathbf{e}}_2}(-v) \sigma_{\hat{\mathbf{e}}_2} = \mathbf{I}. \end{aligned} \quad (30)$$

Now we return to the proposed ansatz for generating a compatible folded configuration. For instance, if $\Omega^{(3)} = \sigma_{\hat{\mathbf{e}}_1} \Omega^{(2)} \subset \text{Orb}_{\mathcal{G}} \Omega^{(q)}$ as proposed, then this implies that

$$\mathbf{Q}_{\hat{\mathbf{e}}_2}(v) \mathbf{Q}_{\hat{\mathbf{b}}_1}(\rho_1) \mathbf{Q}_{\hat{\mathbf{b}}_2}(\phi_2) \mathbf{Q}_{\hat{\mathbf{b}}_3}(\phi_3) = \sigma_{\hat{\mathbf{e}}_1} \mathbf{Q}_{\hat{\mathbf{e}}_2}(v) \mathbf{Q}_{\hat{\mathbf{b}}_1}(-\rho_1) \mathbf{Q}_{\hat{\mathbf{b}}_2}(\phi_2) \sigma_{\hat{\mathbf{e}}_1}. \quad (31)$$

Assume ρ_1, ϕ_2 , and ϕ_3 satisfies (31); further, let $\phi_4 = \phi_2$ and $\phi_5 = \phi_1 = 2\rho_1$. Then, plugging into (30), we obtain

$$\sigma_{\hat{\mathbf{e}}_1} \mathbf{Q}_{\hat{\mathbf{e}}_2}(v) \mathbf{Q}_{\hat{\mathbf{b}}_1}(-\rho_1) \sigma_{\hat{\mathbf{e}}_2} \mathbf{Q}_{\hat{\mathbf{b}}_2}(\phi_6) \sigma_{\hat{\mathbf{e}}_1} \mathbf{Q}_{\hat{\mathbf{b}}_3}(-\phi_7) \mathbf{Q}_{\hat{\mathbf{b}}_2}(-\phi_8) \mathbf{Q}_{\hat{\mathbf{b}}_1}(-\rho_1) \mathbf{Q}_{\hat{\mathbf{e}}_2}(-v) \sigma_{\hat{\mathbf{e}}_2} = \mathbf{I}. \quad (32)$$

Next, let $\phi_6 = \phi_2, \phi_7 = \phi_3$, and $\phi_8 = \phi_2$ (since $\hat{\mathbf{b}}_6 = \mathbf{Q}_{\hat{\mathbf{e}}_3}(\pi) \hat{\mathbf{b}}_2, \hat{\mathbf{b}}_7 = \sigma_{\hat{\mathbf{e}}_2} \hat{\mathbf{b}}_3$, and $\hat{\mathbf{b}}_8 = \sigma_{\hat{\mathbf{e}}_2} \hat{\mathbf{b}}_2$, respectively). Then using (31) again

$$\sigma_{\hat{\mathbf{e}}_1} \mathbf{Q}_{\hat{\mathbf{e}}_2}(v) \mathbf{Q}_{\hat{\mathbf{b}}_1}(-\rho_1) \sigma_{\hat{\mathbf{e}}_2} \mathbf{Q}_{\hat{\mathbf{b}}_1}(-\rho_1) \mathbf{Q}_{\hat{\mathbf{e}}_2}(-v) \sigma_{\hat{\mathbf{e}}_1} \sigma_{\hat{\mathbf{e}}_2} = \mathbf{I}. \quad (33)$$

Recalling $\mathbf{Q}_{\hat{\mathbf{b}}_1}(-\rho_1) = \sigma_{\hat{\mathbf{e}}_2} \mathbf{Q}_{\hat{\mathbf{b}}_1}(\rho_1) \sigma_{\hat{\mathbf{e}}_2}$, $\mathbf{Q}_{\hat{\mathbf{e}}_2}(v) \sigma_{\hat{\mathbf{e}}_2} = \sigma_{\hat{\mathbf{e}}_2} \mathbf{Q}_{\hat{\mathbf{e}}_2}(v)$, and $\sigma_{\hat{\mathbf{e}}_1} \sigma_{\hat{\mathbf{e}}_2} = \sigma_{\hat{\mathbf{e}}_2} \sigma_{\hat{\mathbf{e}}_1}$, we see that equality is indeed obtained in (33), as desired. From this we can conclude that (31) represents a reduced-order, 2 degree of freedom model for the symmetric 8-fold waterbomb. As in previous examples, we can reformulate (31) as an equivalent but simplified form; indeed,

$$\left(\mathbf{Q}_{\hat{\mathbf{e}}_2}(v) \mathbf{Q}_{\hat{\mathbf{b}}_1}(\rho_1) \mathbf{Q}_{\hat{\mathbf{b}}_2}(\phi_2) \hat{\mathbf{b}}_3 \right) \cdot \hat{\mathbf{e}}_1 = 0, \quad (34)$$

is an equivalent condition which can readily be used to solve for $\phi_1 = \phi_1(v, \phi_2) = 2\rho_1(v, \phi_2)$. Then one can solve for the remaining fold angle, ϕ_3 , by computing $\hat{\mathbf{c}}_2 = \mathbf{F}_1 \hat{\mathbf{b}}_2$, $\hat{\mathbf{c}}_3 = \mathbf{F}_2 \hat{\mathbf{b}}_3$, and subsequently, a vector normal to $\Omega^{(2)}$: $\mathbf{n}_2 = \hat{\mathbf{c}}_2 \times \hat{\mathbf{c}}_3$. Lastly,

$$\phi_3 = -\text{sgn}(\mathbf{n}_2 \cdot \hat{\mathbf{e}}_1) \arccos \left(\frac{\mathbf{n}_2 \cdot \sigma_{\hat{\mathbf{e}}_1} \mathbf{n}_2}{|\mathbf{n}_2|^2} \right). \quad (35)$$

To summarize, 1) we choose v and ϕ_2 , 2) solve (34) for ρ_1 , and finally 3) make the assignments

$$\phi_4 = \phi_6 = \phi_8 = \phi_2, \quad \phi_5 = \phi_1 = 2\rho_1, \quad \phi_7 = \phi_3. \quad (36)$$

The solution to (34) is given by

$$\rho_1 = \begin{cases} \begin{cases} \arctan \left(\sqrt{2}\mathcal{F}(\cos \phi_2 - 1) - \mathcal{D}(\cos \phi_2 + 1), \sin \phi_2 (\mathcal{D}\sqrt{2} - \mathcal{F}) \right) & \phi_2 > 0 \\ \arctan \left(-\sqrt{2}\mathcal{F}(\cos \phi_2 - 1) - \mathcal{D}(\cos \phi_2 + 1), -\sin \phi_2 (\mathcal{D}\sqrt{2} + \mathcal{F}) \right) & \phi_2 < 0 \end{cases} \\ \begin{cases} \arctan \left(\sqrt{2}\mathcal{F}(\cos \phi_2 - 1) + \mathcal{D}(\cos \phi_2 + 1), \sin \phi_2 (\mathcal{D}\sqrt{2} + \mathcal{F}) \right) & \phi_2 > 0 \\ \arctan \left(-\sqrt{2}\mathcal{F}(\cos \phi_2 - 1) + \mathcal{D}(\cos \phi_2 + 1), -\sin \phi_2 (\mathcal{D}\sqrt{2} - \mathcal{F}) \right) & \phi_2 < 0 \end{cases} \end{cases} \quad (37)$$

where there are two solution branches given by the pair of equations delimited by the top inner braces and the pair of equations delimited by the bottom inner braces; and where

$$\begin{aligned}\mathcal{D}(v, \phi_2) &:= \sqrt{\sin^2 \phi_2 + 2 \cos \phi_2 - 2 \cos(2v)}, \\ \mathcal{F}(v, \phi_2) &:= |\sin v \sin \phi_2| \cot v.\end{aligned}\tag{38}$$

Consequently, the solution is only real valued (and therefore valid) provided: $\sin^2 \phi_2 + 2 \cos \phi_2 - 2 \cos(2v) \geq 0$. Let $\phi_1 = f_\phi(2\rho)$. Contours of $\phi_1 = \phi_1(v, \phi_2)$ (top row) and $\phi_3 = \phi_3(v, \phi_2)$ (bottom row), for both solutions (folding branch 1 and 2 are the left and right columns, respectively) are shown in fig. 7, as well as example deformed configurations. There are multiple symmetries and other properties of (37) and fig. 7 that should be noted. First, notice that (37) and fig. 7 exhibit flip invariance, as expected, where the “flipping” operation now also includes $v \rightarrow -v$, and a change of folding solution branch. Flip invariance is illustrated in fig. 7 by observing that $(v, \phi_2) \rightarrow (-v, -\phi_2)$ results in a contour of the same magnitude but opposite sign. In the bottom right panel, delimited by a dashed rectangle, we show two folded states which are related by inversion through the origin and change of folding solution branch. Physically, this operation corresponds with flipping the origami over (i.e. reflection via $\sigma_{\hat{\mathbf{e}}_3}$). Second, while there are multiple solutions for $\phi_1 = \phi_1(v, \phi_2)$ (top row), one can be obtained from the other by the change of variables $\phi_2 \rightarrow -\phi_2$; i.e. the contours in branch 2 (right column) are simply the contours of branch 1 (left column) reflected about $\phi_2 = 0$. The contours of $\phi_3 = \phi_3(v, \phi_2)$ (bottom row) have a similar property: we can obtain the branch 2 from branch 1 by reflecting about $v = 0$. Lastly, the condition $\phi_1 \in \mathbb{R}$ (equivalently: $\sin^2 \phi_2 + 2 \cos \phi_2 - 2 \cos(2v) \geq 0$) results in two separate regions for each of the contour plots shown in fig. 7: one where the center vertex of the origami is up (i.e. $v > 0$) and one where it is down (i.e. $v < 0$). The two separate regions only meet at a single point where $\phi_1 = \phi_2 = \dots = \phi_8 = v = 0$, or i.e. the flat configuration. This can be understood as a consequence of the rigidity of the facets. For the vertex to fold with the symmetry of interest and without stretching the facets themselves, it is required that the center vertex flex in some way and, consequently, $v \neq 0$. As alluded to previously, there is a subtle and interesting property of the solutions generated by (34). Because of the symmetry of the underlying vertex and the convention chosen for the deformation map, we have, respectively, that $\hat{\mathbf{b}}_5 = \mathbf{Q}_{\hat{\mathbf{e}}_3}(\pi) \hat{\mathbf{b}}_1$ and $\hat{\mathbf{c}}_5 = \mathbf{Q}_{\hat{\mathbf{e}}_3}(\pi) \hat{\mathbf{c}}_1$; together, these imply that $\hat{\mathbf{c}}_5 = \mathbf{Q}_{\hat{\mathbf{e}}_2}(-v) \hat{\mathbf{b}}_5$. But this was precisely the starting point for constructing solutions for the first half of the vertex with the exception that crease 5 has now taken the place of crease 1 and $v \rightarrow -v$. Let the condition $\Omega = \text{Orb}_{\mathcal{G}} \Omega^{(q)}$ be relaxed. Instead, consider the subgroup $\mathcal{H} = \{\mathbf{I}, \sigma_{\hat{\mathbf{e}}_1}\}$. Recognizing that a compatible folded state of the remaining subset of the vertex can be described by the same reduced order model where crease 5 is analogous to crease 1 and creases 6 through 8 are analogous to creases 2 through 4, we adjust our convention for the deformation map and make the following definitions:

$$\mathbf{F}_i = \begin{cases} \mathbf{Q}_{\hat{\mathbf{e}}_2}(v) \mathbf{Q}_{\hat{\mathbf{b}}_1}(\rho_1), & i = 1, \\ \mathbf{Q}_{\hat{\mathbf{e}}_2}(v) \mathbf{Q}_{\hat{\mathbf{b}}_1}(\rho_1) \prod_{j=2}^i \mathbf{Q}_{\hat{\mathbf{b}}_j}(\phi_j), & 1 < i \leq 4 \\ \mathbf{Q}_{\hat{\mathbf{e}}_2}(-v) \mathbf{Q}_{\hat{\mathbf{b}}_5}(\rho_5) \quad (= \mathbf{F}_4 \mathbf{Q}_{\hat{\mathbf{b}}_5}(\rho_5)), & i = 5, \\ \mathbf{Q}_{\hat{\mathbf{e}}_2}(-v) \mathbf{Q}_{\hat{\mathbf{b}}_5}(\rho_5) \prod_{j=6}^i \mathbf{Q}_{\hat{\mathbf{b}}_j}(\phi_j) \quad (= \mathbf{F}_4 \mathbf{Q}_{\hat{\mathbf{b}}_5}(\rho_5) \prod_{j=6}^i \mathbf{Q}_{\hat{\mathbf{b}}_j}(\phi_j)), & \text{otherwise} \end{cases},\tag{39}$$

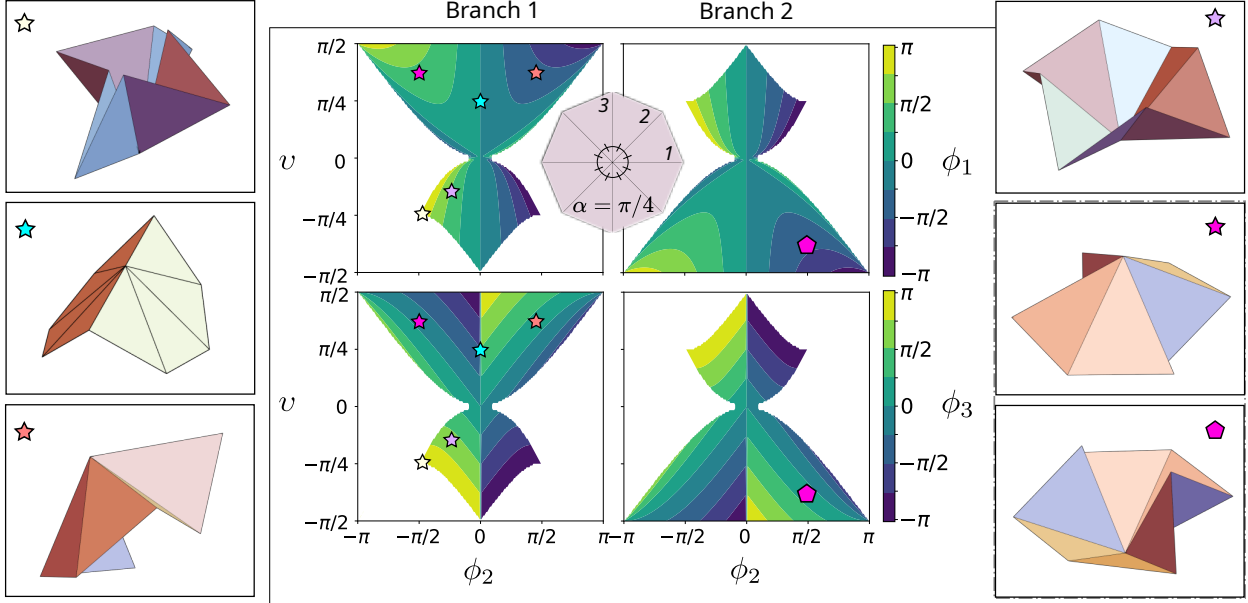


FIG. 7. **Degrees of freedom and kinematics with \mathcal{D}_2 symmetry of a uniform degree 8 vertex.** Contours of $\phi_1 = \phi_1(v, \phi_2)$ (top row) and $\phi_3 = \phi_3(v, \phi_2)$ (bottom row), and example folded states of a uniform degree 8 vertex such that the folded states satisfy the symmetry corresponding to the group $\langle \sigma_{\hat{e}_2}, \mathbf{Q}_{\hat{e}_3}(\pi) \rangle$. White regions of the contour plots signify parts of the (v, ϕ_2) domain which are inadmissible; that is, a folded configuration with the specified (v, ϕ_2) and symmetry cannot be attained. The admissible space consists of two distinct regions connected only at the flat state (i.e. the origin). Physically, for there to be any folding about any of the creases without stretching the facets themselves, it is required that the center vertex flex in some way. When a point is inverted about the origin and moved to the other folding solution branch, ϕ_1 and ϕ_3 have the same magnitude but opposite sign, which means the solutions satisfy flip invariance.

and

$$\begin{aligned} \Omega_0^{(r)} &:= \Omega_0^{(5)} \cup \Omega_0^{(6)}, & \Omega^{(r)} &:= \Omega^{(5)} \cup \Omega^{(6)} \\ \Omega_0^{(\ell)} &:= \text{Orb}_{\mathcal{G}} \Omega_0^{(r)}, & \Omega^{(\ell)} &:= \text{Orb}_{\mathcal{G}} \Omega^{(r)} \end{aligned} \quad (40)$$

Given (39), we can generate a compatibly folded state *with less symmetry than \mathcal{D}_2* by

1. specifying v and ϕ_2 ,
2. solving for ρ_1 and ϕ_3 using (37) (and the deformation map),
3. specifying ϕ_6 ,
4. solving for ρ_5 and ϕ_7 , again using (37) with appropriate analogs (e.g. crease 1 \rightarrow crease 5, crease 2 \rightarrow crease 6, etc.), and
5. making the assignments

$$\phi_1 = \phi_5 = \rho_1 + \rho_5, \quad \phi_4 = \phi_2, \quad \phi_8 = \phi_6. \quad (41)$$

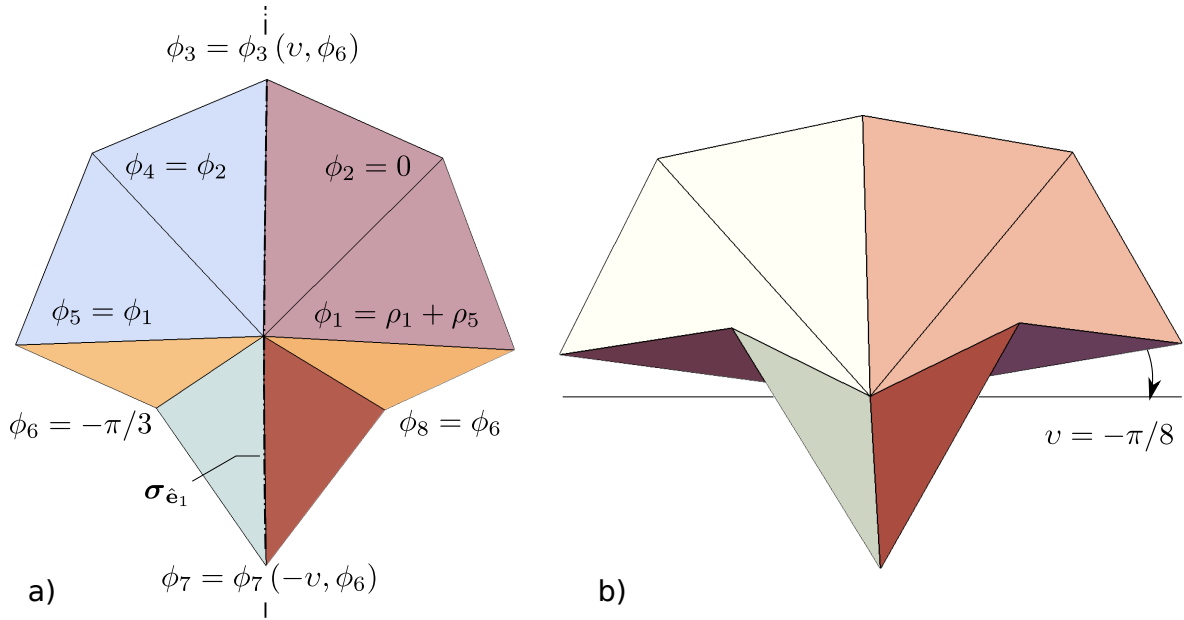


FIG. 8. **Constructing compatibly folded states with symmetry breaking.** a) Leveraging the solution of the reduced order model with two degrees of freedom (i.e. v and ϕ_2) to generate a solution with less symmetry and three degrees of freedom. In this example, $v = -\pi/8$, $\phi_2 = 0$, and $\phi_6 = -\pi/3 \neq \phi_2$. b) Alternate view.

Through this procedure we have leveraged the solution of a reduced order model with two degrees of freedom (i.e. v and ϕ_2) to generate a solution with less symmetry and three degrees of freedom (i.e. v , ϕ_2 and ϕ_6). Note that the symmetry is now described by $\mathcal{H} \leq \mathcal{G}$ such that we have broken the symmetry associated with the $\sigma_{\hat{e}_2}$ transformation. As we will see in future developments, this procedure generalizes to all of the examples that we consider where the folded state has both reflection and rotational symmetries. It represents an analytical tool for generating families of solutions, generally with less symmetry and often with more degrees of freedom, from a simpler, lower dimensional equation. An example folded configuration of the symmetric 8-fold vertex generated by this procedure is shown in fig. 8.

B. Generalized reflection-rotations

Next we are interested in how the method developed in section V A can be generalized to vertices with symmetries described by groups, \mathcal{G} , where $\mathcal{G} = \langle \sigma_{\hat{e}_2}, \mathbf{Q}_{\hat{e}_3}(\varphi) \rangle$ for general angle φ ⁶. First, note that for \mathcal{G} to satisfy the closure property, we need $\mathbf{Q}_{\hat{e}_3}^m(\varphi) = \mathbf{I}$ for some $m \in \mathbb{Z}$. In addition, the choice of deformation map and overall approach used to derive (34) made use of the fact that the two planes of reflection symmetries cut through creases of the vertex (e.g. creases, 1, 3, 5, and 7.). This can always be done provided $\varphi = 2\pi/2h$, and, consequently, $\mathcal{G} = \mathcal{D}_{2h}$ where $h \in \mathbb{N}$ and \mathcal{D}_{2h} is the group of symmetries of a regular polygon

⁶

If $\mathcal{G} = \langle \sigma_{\hat{e}_2}, \mathbf{Q}_{\hat{e}_3}(\varphi) \rangle$, then this implies that there are also reflection symmetries about planes normal to $\mathbf{Q}_{\hat{e}_3}^m(\varphi/2)\hat{e}_2$ for all $m \in \{j \in \mathbb{N} : j \leq \pi/\varphi\}$.

of $2h$ sides. To this end, let $\varphi = 2\pi/2h, h \in \mathbb{N}$, $\hat{\mathbf{b}}_k = \mathbf{Q}_{\hat{\mathbf{e}}_3}(\varphi/2) \hat{\mathbf{b}}_1$ (i.e. $\sigma_{\hat{\mathbf{b}}_k \times \hat{\mathbf{e}}_3} \in \mathcal{G}$), and $\Omega_0^{(c)} = \bigcup_{i=1}^{k-1} \Omega_0^{(i)}$, where $\Omega_0^{(c)} \subset \Omega_0$ is the unit cell to be folded such that $\Omega = \text{Orb}_{\mathcal{G}} \Omega^{(c)}$. Then

$$\frac{\hat{\mathbf{c}}_k \cdot \hat{\mathbf{e}}_2}{\hat{\mathbf{c}}_k \cdot \hat{\mathbf{e}}_1} = \frac{\left(\mathbf{F}_{k-1}(v, \phi_1, \dots, \phi_{k-1}) \hat{\mathbf{b}}_k \right) \cdot \hat{\mathbf{e}}_2}{\left(\mathbf{F}_{k-1}(v, \phi_1, \dots, \phi_{k-1}) \hat{\mathbf{b}}_k \right) \cdot \hat{\mathbf{e}}_1} = \frac{\hat{\mathbf{b}}_k \cdot \hat{\mathbf{e}}_2}{\hat{\mathbf{b}}_k \cdot \hat{\mathbf{e}}_1}, \quad (42)$$

represents a reduced-order model for solutions to (6) with \mathcal{D}_{2h} symmetry where, when the convention chosen for the deformation map is given by (28), the axis of rotation for the rotational symmetries is $\hat{\mathbf{e}}_3$ and the normal vectors for each of the planes of reflection are orthogonal to $\hat{\mathbf{e}}_3$. In principle, one 1) solves (42) for $\phi_1 = \phi_1(v, \phi_2, \dots, \phi_{k-1})$, then 2) solves for ϕ_k by⁷

$$\phi_k = -\text{sgn} \left(\mathbf{n}_{k-1} \cdot \left(\hat{\mathbf{b}}_k \times \hat{\mathbf{e}}_3 \right) \right) \arccos \left(\frac{\mathbf{n}_{k-1} \cdot \sigma_{\hat{\mathbf{b}}_k \times \hat{\mathbf{e}}_3} \mathbf{n}_{k-1}}{|\mathbf{n}_{k-1}|^2} \right), \quad (43)$$

$$\mathbf{n}_{k-1} = \hat{\mathbf{c}}_{k-1} \times \hat{\mathbf{c}}_k,$$

and finally 3) makes the assignments

$$\phi_{k+1} = \phi_{k-1}, \phi_{k+2} = \phi_{k-2}, \dots, \phi_{2k-1} = \phi_1, \phi_{2k} = \phi_2, \phi_{2k+1} = \phi_3, \dots, \text{etc.}; \quad (44)$$

in other words, after crease k , going counterclockwise around the vertex, the fold angles are assigned in decreasing order until 1, then increasing order until k , then decreasing until 1, ..., etc., until all of the fold angles have been assigned. For the example considered in section V A, we had $k = 3$, $\varphi = \pi$ and the sequence of fold angle assignments went $(\phi_1, \dots, \phi_8) = (\phi_1, \phi_2, \phi_3, \phi_2, \phi_1, \phi_2, \phi_3, \phi_2)$.

As a simple example of this generalization, consider searching for compatible, folded states of the symmetric 8-fold vertex such that $\varphi = \pi/2$ —which is the most symmetry for folded configurations that the vertex admits: \mathcal{D}_4 . In this case, $k = 2$ and $\Omega_0^{(c)} = \Omega_0^{(1)}$. Using (18) and (43), one obtains

$$(\phi_1, \phi_2) = \begin{cases} \left(2 \arccos \left(\frac{|\sqrt{2}+2(1-2H(v)) \cos v|}{2+\sqrt{2}(1-2H(v)) \cos v} \right), -2|v| \right), & \phi_1 \text{ valley, } \phi_2 \text{ mountain} \\ \left(-2 \arccos \left(\frac{|\sqrt{2}-2(1-2H(v)) \cos v|}{2-\sqrt{2}(1-2H(v)) \cos v} \right), 2|v| \right), & \text{vice versa} \end{cases}, \quad (45)$$

where $H(x) = (x + |x|)/2x$, is the Heaviside step function.

The last step then is to make the assignments $(\phi_1, \dots, \phi_8) = (\phi_1, \phi_2, \phi_1, \phi_2, \phi_1, \phi_2, \phi_1, \phi_2)$. This recovers the well-known solution for the “fully-symmetric” folding of the 8-fold waterbomb where the crease assignments are alternating mountain and valley [29]. For the first solution in (45), the odd creases are valley and the even creases are mountain; for the second, vice versa. More details on this kinematic description of the 8-fold waterbomb, its multistability when the creases store elastic energy, and various other interesting properties can be found in [29, 31, 67].

⁷ The sign term adheres to the mountain-valley convention by recognizing that if a crease lies within a plane of reflection, it is mountain if the normal of its right facet shares a similar direction with the normal to the plane of symmetry (provided the sign of the normal is chosen as in (43)).

Notice that, in assigning fold angles around the vertex, the sequence of indices on the right side of the assignment were increasing twice for the \mathcal{D}_2 folding and four times for the \mathcal{D}_4 folding; in addition, for each of the foldings with \mathcal{D}_1 folding (i.e. a single reflection symmetry), the sequence of indices is increasing once. In general, the sequence of indices for \mathcal{D}_{2h} foldings will increase $2h$ times. Similarly, $2h$ is the number of times that the condition (42) is needed to be substituted into (6) in order to show that the reduced order solution does indeed satisfy compatibility. This, in addition to the introduction of the parameter v , all corresponds with a reduction of degrees of freedom from $N - 3$ to N/m , where m is the smallest integer such that $\mathbf{Q}_{\mathbf{e}_3}^m(\varphi) = \mathbf{I}$, i.e. m is the order of the generating rotation.

C. General 8-vertex with \mathcal{D}_2 symmetry

As a simple example of this generalization, an 8-fold vertex such that $\alpha_1 = \alpha, \alpha_2 = \pi/2 - \alpha$, and $\mathcal{G} = \langle \sigma_{\mathbf{e}_2}, \mathbf{Q}_{\mathbf{e}_3}(\pi/2) \rangle$, as shown in fig. 9.a. Then, using (42), we obtain

$$\rho_1 = \left\{ \begin{array}{l} \left\{ \begin{array}{l} \arctan \left(\begin{array}{l} \mathcal{K} \cos \alpha (\cos \phi_2 - 1) - \mathcal{J} (\cos^2 \alpha \cos \phi_2 + \sin^2 \alpha), \\ \cos \alpha \sin \phi_2 \mathcal{J} - \mathcal{K} (\cos^2 \alpha \cos \phi_2 + \sin^2 \alpha) \tan \left(\frac{\phi_2}{2} \right) \end{array} \right), \quad \phi_2 > 0 \\ - \arctan \left(\begin{array}{l} -\mathcal{K} \cos \alpha (\cos \phi_2 - 1) - \mathcal{J} (\cos^2 \alpha \cos \phi_2 + \sin^2 \alpha), \\ -\cos \alpha \sin \phi_2 \mathcal{J} - \mathcal{K} (\cos^2 \alpha \cos \phi_2 + \sin^2 \alpha) \tan \left(\frac{\phi_2}{2} \right) \end{array} \right), \quad \phi_2 < 0 \end{array} \right\} \\ \left\{ \begin{array}{l} - \arctan \left(\begin{array}{l} \mathcal{K} \cos \alpha (\cos \phi_2 - 1) + \mathcal{J} (\cos^2 \alpha \cos \phi_2 + \sin^2 \alpha), \\ \cos \alpha \sin \phi_2 \mathcal{J} + \mathcal{K} (\cos^2 \alpha \cos \phi_2 + \sin^2 \alpha) \tan \left(\frac{\phi_2}{2} \right) \end{array} \right), \quad \phi_2 > 0 \\ \arctan \left(\begin{array}{l} -\mathcal{K} \cos \alpha (\cos \phi_2 - 1) + \mathcal{J} (\cos^2 \alpha \cos \phi_2 + \sin^2 \alpha), \\ -\cos \alpha \sin \phi_2 \mathcal{J} + \mathcal{K} (\cos^2 \alpha \cos \phi_2 + \sin^2 \alpha) \tan \left(\frac{\phi_2}{2} \right) \end{array} \right), \quad \phi_2 < 0 \end{array} \right\} \end{array} \right. \quad (46)$$

where

$$\mathcal{J}(v, \phi_2) := \sqrt{5 - 8 \cos v + 4 \cos \phi_2 - \cos(2\phi_2) + 8 \cos(4\alpha) \sin^4 \left(\frac{\phi_2}{2} \right)}, \quad (47)$$

$$\mathcal{K}(v, \phi_2) := 4 |\cos \alpha \sin v \sin \phi_2| \sin \alpha \cot v,$$

and, consequently, the solution is only real valued (and therefore valid) provided: $\mathcal{J} \in \mathbb{R}$. Example folded states for $v = \pi/4, \phi_2 = \pi/3$ and $\alpha_1 = \pi/8$ (top row) and $\alpha_1 = 3\pi/8$ (bottom row) for the first (left column) and second (right column) folding branches are shown in

fig. 9.b. Let $\phi_1 = f_\phi(2\rho_1(v, \phi_2))$. The contours for ϕ_1 (top row) and $\phi_3 = \phi_3(v, \phi_2)$ (bottom row) are shown in fig. 9.c for $\alpha_1 = \pi/8$ (left column) and $\alpha_1 = 3\pi/8$ (right column). There are several notable features about the \mathcal{D}_2 kinematics of the degree 8 vertex with varying α_1 :

- 1) When $\alpha_1 < \pi/4$, creases $\{1, 2, 8\}$ and $\{3, 4, 5\}$ are nearer to each other than either of collinear creases 3 and 7. The left column of fig. 9.c ($\alpha_1 = \pi/8$) shows that, when creases 1 and 2 are nearer to each other, ϕ_1 folds primarily as a function of ϕ_2 and is almost independent of the elevation angle, v . In contrast, ϕ_3 has a stronger dependence on v and only folds flat as $|v| \rightarrow \pi/2$.
- 2) Alternatively, when $\alpha_1 > \pi/4$, creases $\{2, 3, 4\}$ and $\{6, 7, 8\}$ are nearer to each other than either of collinear creases 1 and 5. By the right column (and top row) of fig. 9.c ($\alpha_1 = 3\pi/8$), one can see that ϕ_1 folds less as a function of v and ϕ_2 ; i.e. $|\phi_1| \leq \pi/2$ for much of the $(v, \phi_2) \in [-\pi/2, \pi/2] \times [-\pi, \pi]$ domain. In contrast, the contours of ϕ_3 take the form of thin, linear bands with slope of unity (i.e. along lines of $v = \phi_2 + \text{const.}$)—which suggests that ϕ_3 folds more as a function of (v, ϕ_2) when $\alpha_1 \rightarrow \pi/2$. See fig. 9, for example.
- 3) FIG. 9.d shows inadmissible regions are delineated by a black dashed line when no solution exists and a red dash-dot line when the region is inadmissible due to contact. Note that more of the domain has a folding solution as $|\alpha_1 - \pi/4|$ increases. In other words, the condition $\mathcal{J} \in \mathbb{R}$ (i.e. $5 - 8 \cos v + 4 \cos \phi_2 - \cos(2\phi_2) + 8 \cos(4\alpha) \sin^4(\frac{\phi_2}{2}) \geq 0$) is met for a greater part of the domain as $|\alpha_1 - \pi/4|$ increases. Physically, as creases in the vertex either collect nearer to 1 and 4 ($\alpha_1 < \pi/4$) or nearer to 3 and 7 ($\alpha_1 > \pi/4$), the center vertex does not need to flex up or down as much in order to allow folding about crease 2. In terms of contact, more of the domain becomes inadmissible as $|\alpha_1 - \pi/4|$. This may be due, in part, to the fact that the minimum distances between pairs of faces in the flat state is decreasing (i.e. there is a smaller minimum sector angle). An animation of an $\alpha_1 = \pi/6$ vertex folding through 1) configuration space into admissible regions, 2) regions where no solution exists, and 3) regions where contact occurs, is shown in Animation #5 included in the ESI.

VI. CONCLUSION

The Lagrangian approach to origami makes the deformation map the fundamental kinematic description of the origami. Here we showed its advantages toward exploiting symmetry via reduced order compatibility conditions. The reduced order conditions were solved exactly for multi-degree of freedom kinematics of symmetric degree 6 and degree 8 vertices. It is expected that the exact solutions will facilitate and inspire new origami design algorithms. While the results herein were restricted to single vertices with an even number of creases, the developed approach should generalize readily to multivertex crease patterns and odd degree vertices. For instance, globally compatible solutions for a multivertex crease pattern can be obtained by solving for local compatibility at each of the vertices and then enforcing that, where vertices share a crease, the corresponding fold angle agrees. For odd degree vertices, one could, in principle, add a “pseudo” crease that (agrees with the symmetry of interest and) results in an even degree vertex that has a reduced order compatibility condition already

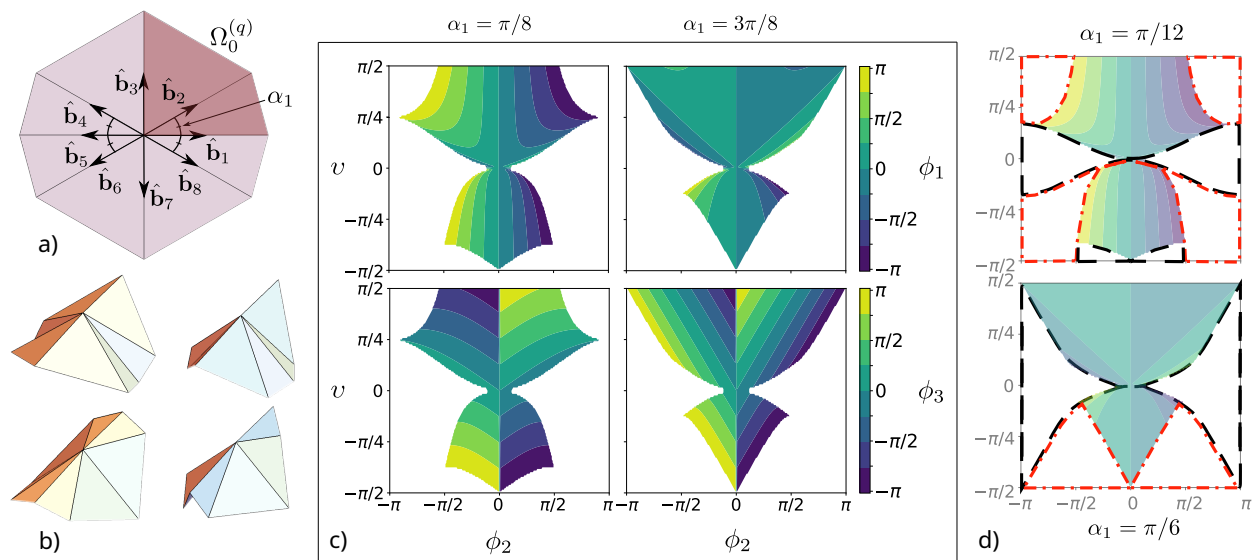


FIG. 9. **Kinematics of a degree 8 vertex with \mathcal{D}_2 symmetry and variable α_1 .** a) Geometry of degree 8 vertex with \mathcal{D}_2 symmetry parameterized by α_1 . b) Example folded configurations for $\alpha_1 = \pi/8$ (top row) and $\alpha_1 = 3\pi/8$ (bottom row). c) Contours of $\phi_1 = \phi_1(v, \phi_2)$ (top row) and $\phi_3 = \phi_3(v, \phi_2)$ (bottom row) for $\alpha_1 = \pi/8$ (left column) and $\alpha_1 = 3\pi/8$ (right column). d) The admissible part of the (v, ϕ_2) for $\alpha = \pi/12$ (top) and $\alpha_1 = \pi/6$ (bottom) where inadmissible regions are delineated by a black dashed line when no solution exists and a red dash-dot line when the region is inadmissible due to contact. More of the domain has a folding solution as $|\alpha_1 - \pi/4|$ increases, but more of the domain is also inadmissible due to contact.

outlined in this work. Then the odd degree vertex solution could be obtained by subsequently solving for the fold angle of the pseudo crease as zero. While these generalizations are straight forward, it is possible that different generalizations can be made which are more amenable to exact solution or more computationally efficient, which presents an interesting topic for future work.

In this study, we limited our analysis to origami structures with negligible thickness. Finite thickness origami structures are an important class of foldable systems with many practical advantages. Novel hinge concepts [76, 77] and fold topology strategies [78, 79] are effective approaches to address this challenge. One of the consequences of thick systems is that self-contact at the hinge constrains the kinematic range of folding, often only allowing folding in one direction from the flat state. In light of this, incorporating finite thickness into our analysis would likely reduce the domain of accessible folding kinematics we presented. Extending our Lagrangian formulation to accommodate thickness is another potential direction for future study.

ACKNOWLEDGEMENTS

We are grateful to Richard James and Kaushik Bhattacharya for many insightful discussions. We acknowledge the support of the Laboratory University Collaboration Initiative sponsored by the US Office of the Secretary of Defence and the support of the Air Force

Appendix A: Algebraic perspective of the 4-vertex with reflection symmetry

For the 4 vertex with reflection symmetry, (12) takes the form

$$\mathbf{Q}_{\hat{\mathbf{b}}_1}(\phi_1) \mathbf{Q}_{\hat{\mathbf{b}}_2}(\phi_2) \mathbf{Q}_{\hat{\mathbf{b}}_3}(\phi_3) \mathbf{Q}_{\sigma_{\hat{\mathbf{e}}_2} \hat{\mathbf{b}}_2}(\phi_4) = \mathbf{I}. \quad (\text{A1})$$

Using (13a), (13d), and (13e), this can be rewritten as

$$\mathbf{Q}_{\hat{\mathbf{b}}_1} \left(\frac{\phi_1}{2} \right) \mathbf{Q}_{\hat{\mathbf{b}}_2}(\phi_2) \mathbf{Q}_{\hat{\mathbf{b}}_3}(\phi_3) \sigma_{\hat{\mathbf{e}}_2} \left(\mathbf{Q}_{\hat{\mathbf{b}}_2}(-\phi_4) \mathbf{Q}_{\hat{\mathbf{b}}_1} \left(-\frac{\phi_1}{2} \right) \right) \sigma_{\hat{\mathbf{e}}_2} = \mathbf{I}. \quad (\text{A2})$$

Notice that, if one can work the first part of the product, namely $\mathbf{Q}_{\hat{\mathbf{b}}_1}(\phi_1/2) \mathbf{Q}_{\hat{\mathbf{b}}_2}(\phi_2)$, in between the $\sigma_{\hat{\mathbf{e}}_2}$ and $\sigma_{\hat{\mathbf{e}}_2}$ transformations, then terms cancel through appropriate choice of ϕ_4 . To accomplish this, recall the notion of constructing a compatible folded state as the orbit of $\Omega^{(h)}$ (fig. 1). In this case, by construction, $\Omega^{(3)} = \sigma_{\hat{\mathbf{e}}_2} \Omega^{(2)}$ and $\Omega^{(4)} = \sigma_{\hat{\mathbf{e}}_2} \Omega^{(1)}$. This implies that

$$\mathbf{Q}_{\hat{\mathbf{b}}_1} \left(\frac{\phi_1}{2} \right) \mathbf{Q}_{\hat{\mathbf{b}}_2}(\phi_2) \mathbf{Q}_{\hat{\mathbf{b}}_3}(\phi_3) = \sigma_{\hat{\mathbf{e}}_2} \mathbf{Q}_{\hat{\mathbf{b}}_1} \left(\frac{\phi_1}{2} \right) \mathbf{Q}_{\hat{\mathbf{b}}_2}(\phi_2) \sigma_{\hat{\mathbf{e}}_2}, \quad (\text{A3a})$$

$$\mathbf{Q}_{\hat{\mathbf{b}}_1} \left(\frac{\phi_1}{2} \right) \mathbf{Q}_{\hat{\mathbf{b}}_2}(\phi_2) \mathbf{Q}_{\hat{\mathbf{b}}_3}(\phi_3) \mathbf{Q}_{\hat{\mathbf{b}}_4}(\phi_4) = \mathbf{Q}_{\hat{\mathbf{b}}_1} \left(-\frac{\phi_1}{2} \right) = \sigma_{\hat{\mathbf{e}}_2} \mathbf{Q}_{\hat{\mathbf{b}}_1} \left(\frac{\phi_1}{2} \right) \sigma_{\hat{\mathbf{e}}_2}, \quad (\text{A3b})$$

respectively. The second condition, (A3b), is trivially satisfied (by (13e)). The first condition, (A3a), can be satisfied by proper choice of ϕ_1 , ϕ_2 and ϕ_3 . Assuming (A3a) holds, we see that (A2) takes the form

$$\mathbf{Q}_{\hat{\mathbf{b}}_1} \left(\frac{\phi_1}{2} \right) \mathbf{Q}_{\hat{\mathbf{b}}_2}(\phi_2 - \phi_4) \mathbf{Q}_{\hat{\mathbf{b}}_1} \left(-\frac{\phi_1}{2} \right) = \mathbf{I}, \quad (\text{A4})$$

which is satisfied if and only if $\phi_4 = \phi_2$, consistent with the assumed symmetry of the folded configuration. Thus, (A3a) represents a dimensionally reduced form of (6). By (13e), the ansatz $\mathbf{Q}_{\hat{\mathbf{b}}_1}(\phi_1/2) \mathbf{Q}_{\hat{\mathbf{b}}_2}(\phi_2) = \mathbf{Q}_{\hat{\mathbf{e}}_2}(\varphi) \mathbf{Q}_{\hat{\mathbf{b}}_3}(\varphi')$ can be used to readily solve (A3a)—which is equivalent to the condition given in (9) that was developed from the geometric perspective. Upon using this ansatz and then backward substitution, one finds that $\phi_3 = -\phi_1$.

Appendix B: Self-contact detection procedure

Solutions to the compatibility conditions formulated in this work (and others) do not consider self-contact. Detecting contact can be expensive [80], but we find here that the Lagrangian approach—along with analytical solutions—provides a path forward. Using the deformation map, one can readily determine the locations of the facets in the folded configuration. Intersection of a line with a triangle, in 3 dimensions, can be checked for in a straight forward manner. Let \mathbf{q}_1 and \mathbf{q}_2 denote the end points of the line and \mathbf{p}_1 , \mathbf{p}_2 , and \mathbf{p}_3 denote the vertices of the triangle. Given 4 points, $\mathbf{y}_1, \dots, \mathbf{y}_4$, the signed volume of the tetrahedron determined by the points is

$$\mathcal{V}(\mathbf{x}_1, \mathbf{x}_2, \mathbf{x}_3, \mathbf{x}_4) = \frac{1}{6} ((\mathbf{y}_2 - \mathbf{y}_1) \times (\mathbf{y}_3 - \mathbf{y}_1)) \cdot (\mathbf{y}_4 - \mathbf{y}_1). \quad (\text{B1})$$

If the $\mathcal{V}(\mathbf{q}_1, \mathbf{p}_1, \mathbf{p}_2, \mathbf{p}_3)$ and $\mathcal{V}(\mathbf{q}_2, \mathbf{p}_1, \mathbf{p}_2, \mathbf{p}_3)$ are *different* signs, then the line passes through the plane of the triangle; and if $\mathcal{V}(\mathbf{q}_1, \mathbf{q}_2, \mathbf{p}_1, \mathbf{p}_2)$, $\mathcal{V}(\mathbf{q}_1, \mathbf{q}_2, \mathbf{p}_2, \mathbf{p}_3)$, $\mathcal{V}(\mathbf{q}_1, \mathbf{q}_2, \mathbf{p}_3, \mathbf{p}_1)$, are all the same sign, then the line lies in the (infinite) extrusion of the triangle normal to its plane. Thus, if both conditions are met, the line and triangle intersect. For instance, to check for self-contact in the 6 vertex with reflection symmetry, we consider the following

- 1) if any $\hat{\mathbf{c}}_i \cdot \hat{\mathbf{e}}_2 < 0$ for $i = 1, \dots, 4$, then, by symmetry, self-contact has occurred;
- 2) each pair of lines and facets in $\Omega^{(1)} \cup \Omega^{(2)} \cup \Omega^{(3)}$ are checked for intersection by signed volumes of the corresponding tetrahedrons. To be precise, there is an intersection between a facet and facet edge pair if and only if

$$\begin{aligned} \text{sgn}(\mathcal{V}(\mathbf{q}_1, \mathbf{p}_1, \mathbf{p}_2, \mathbf{p}_3)) &\neq \text{sgn}(\mathcal{V}(\mathbf{q}_2, \mathbf{p}_1, \mathbf{p}_2, \mathbf{p}_3)) && \text{and} \\ \text{sgn}(\mathcal{V}(\mathbf{q}_1, \mathbf{q}_2, \mathbf{p}_1, \mathbf{p}_2)) &= \text{sgn}(\mathcal{V}(\mathbf{q}_1, \mathbf{q}_2, \mathbf{p}_2, \mathbf{p}_3)) = \text{sgn}(\mathcal{V}(\mathbf{q}_1, \mathbf{q}_2, \mathbf{p}_3, \mathbf{p}_1)). \end{aligned} \quad (\text{B2})$$

If an intersection between any pair of lines and facets occur, we say contact has occurred and the configuration is inadmissible.

Alternative algorithms for detecting contact that are likely more efficient can be found in [80, 81]. Despite the relative expense of the contact problem, we can still efficiently map out the admissible regions of configuration space where the structure is folded symmetrically in minutes (as opposed to hours or days). This efficiency comes from several factors 1) we have closed form solutions for the fold angles in hand, 2) we can directly obtain the deformation map from the Lagrangian approach and fold angles, and 3) the symmetry of the deformed configurations simplifies the contact problem.

When self-contact occurs will depend on the geometry of the facets of the origami. In this work, all facet geometries are chosen such that all of the creases are the same length, and outer edges are added between neighboring creases to form triangular facets. Although the procedure outlined herein is specific to triangular facets, it can readily be extended to facets of general shape by first approximating the shape of each facet using a triangulation procedure.

-
- [1] Mark Schenk, Andrew D Viquerat, Keith A Seffen, and Simon D Guest. Review of inflatable booms for deployable space structures: packing and rigidization. *Journal of Spacecraft and Rockets*, 51(3):762–778, 2014.
 - [2] Shannon A Zirbel, Robert J Lang, Mark W Thomson, Deborah A Sigel, Phillip E Walkemeyer, Brian P Trease, Spencer P Magleby, and Larry L Howell. Accommodating thickness in origami-based deployable arrays. *Journal of Mechanical Design*, 135(11), 2013.
 - [3] Anthony Verzoni and Masoud Rais-Rohani. Transition analysis of flat-foldable origami-inspired deployable shelter concepts. *Engineering Structures*, 273:115074, 2022.
 - [4] David Melancon, Benjamin Gorissen, Carlos J García-Mora, Chuck Hoberman, and Katia Bertoldi. Multistable inflatable origami structures at the metre scale. *Nature*, 592(7855): 545–550, 2021.
 - [5] Kaori Kuribayashi, Koichi Tsuchiya, Zhong You, Dacian Tomus, Minoru Umemoto, Takahiro Ito, and Masahiro Sasaki. Self-deployable origami stent grafts as a biomedical application of

- ni-rich tiny shape memory alloy foil. *Materials Science and Engineering: A*, 419(1-2):131–137, 2006.
- [6] Ebbe S Andersen, Mingdong Dong, Morten M Nielsen, Kasper Jahn, Ramesh Subramani, Wael Mamdouh, Monika M Golas, Bjoern Sander, Holger Stark, Cristiano LP Oliveira, Jan S Pedersen, Victoria Birkedal, Flemming Besenbacher, Kurt Gothelf, and Jørgen Kjems. Self-assembly of a nanoscale DNA box with a controllable lid. *Nature*, 459(7243):73–76, 2009.
- [7] Prasanth Velvaluri, Arun Soor, Paul Plucinsky, Rodrigo Lima de Miranda, Richard D James, and Eckhard Quandt. Origami-inspired thin-film shape memory alloy devices. *Scientific reports*, 11(1):10988, 2021.
- [8] Qiao Jiang, Shaoli Liu, Jianbing Liu, Zhen-Gang Wang, and Baoquan Ding. Rationally designed dna-origami nanomaterials for drug delivery in vivo. *Advanced Materials*, 31(45):1804785, 2019.
- [9] Xiao Rui Liu, Iong Ying Loh, Winna Siti, Hon Lin Too, Tommy Anderson, and Zhisong Wang. A light-operated integrated dna walker–origami system beyond bridge burning. *Nanoscale Horizons*, 8(6):827–841, 2023.
- [10] Jeong-Hyun Cho, Michael D Keung, Niels Verellen, Liesbet Lagae, Victor Moshchalkov, Pol Van Dorpe, and David H Gracias. Nanoscale origami for 3d optics. *Small*, 7(14):1943–1948, 2011.
- [11] Matthew Grasinger and Pradeep Sharma. Thermal fluctuations (eventually) unfold nanoscale origami. *Journal of the Mechanics and Physics of Solids*, page 105527, 2024. ISSN 0022-5096.
- [12] Larissa S Novelino, Qiji Ze, Shuai Wu, Glaucio H Paulino, and Ruike Zhao. Untethered control of functional origami microrobots with distributed actuation. *Proceedings of the National Academy of Sciences*, 117(39):24096–24101, 2020.
- [13] Shuai Wu, Qiji Ze, Jize Dai, Nupur Udipi, Glaucio H Paulino, and Ruike Zhao. Stretchable origami robotic arm with omnidirectional bending and twisting. *Proceedings of the National Academy of Sciences*, 118(36), 2021.
- [14] Sahand Sadeghi, Samuel R Allison, Blake Bestill, and Suyi Li. Tmp origami jumping mechanism with nonlinear stiffness. *Smart Materials and Structures*, 30(6):065002, 2021.
- [15] Priyanka Bhovad, Joshua Kaufmann, and Suyi Li. Peristaltic locomotion without digital controllers: Exploiting multi-stability in origami to coordinate robotic motion. *Extreme Mechanics Letters*, 32:100552, 2019.
- [16] S Li, H Fang, and KW Wang. Recoverable and programmable collapse from folding pressurized origami cellular solids. *Physical Review Letters*, 117(11):114301, 2016.
- [17] Clark C Addis, Salvador Rojas, and Andres F Arrieta. Connecting the branches of multistable non-euclidean origami by crease stretching. *Physical Review E*, 108(5):055001, 2023.
- [18] Benjamin Treml, Andrew Gillman, Philip Buskohl, and Richard Vaia. Origami mechanologic. *Proceedings of the National Academy of Sciences*, 115(27):6916–6921, 2018.
- [19] Théo Jules, Austin Reid, Karen E Daniels, Muhittin Mungan, and Frédéric Lechenault. Delicate memory structure of origami switches. *Physical Review Research*, 4(1):013128, 2022.
- [20] Priyanka Bhovad and Suyi Li. Physical reservoir computing with origami and its application to robotic crawling. *Scientific Reports*, 11(1):1–18, 2021.
- [21] Elisa Boatti, Nikolaos Vasios, and Katia Bertoldi. Origami metamaterials for tunable thermal expansion. *Advanced Materials*, 29(26):1700360, 2017.
- [22] Ke Liu, Phanisri P Pratapa, Diego Misseroni, Tomohiro Tachi, and Glaucio H Paulino. Triclinic metamaterials by tristable origami with reprogrammable frustration. *Advanced Materials*, 34

- (43):2107998, 2022.
- [23] Yasuhiro Miyazawa, Hiromi Yasuda, Hyungkyu Kim, James H Lynch, Kosei Tsujikawa, Takahiro Kunimine, Jordan R Raney, and Jinkyu Yang. Heterogeneous origami-architected materials with variable stiffness. *Communications Materials*, 2(1):1–7, 2021.
 - [24] Diego Misseroni, Phanisri P Pratapa, Ke Liu, and Glaucio H Paulino. Experimental realization of tunable poisson’s ratio in deployable origami metamaterials. *Extreme Mechanics Letters*, 53:101685, 2022.
 - [25] Zirui Zhai, Yong Wang, Ken Lin, Lingling Wu, and Hanqing Jiang. In situ stiffness manipulation using elegant curved origami. *Science advances*, 6(47):eabe2000, 2020.
 - [26] Jesse L Silverberg, Arthur A Evans, Lauren McLeod, Ryan C Hayward, Thomas Hull, Christian D Santangelo, and Itai Cohen. Using origami design principles to fold reprogrammable mechanical metamaterials. *science*, 345(6197):647–650, 2014.
 - [27] Mark Schenk and Simon D Guest. Geometry of miura-folded metamaterials. *Proceedings of the National Academy of Sciences*, 110(9):3276–3281, 2013.
 - [28] Bin Liu, Jesse L Silverberg, Arthur A Evans, Christian D Santangelo, Robert J Lang, Thomas C Hull, and Itai Cohen. Topological kinematics of origami metamaterials. *Nature Physics*, 14(8): 811–815, 2018.
 - [29] Matthew Grasinger, Andrew Gillman, and Philip R Buskohl. Multistability, symmetry and geometric conservation in eightfold waterbomb origami. *Proceedings of the Royal Society A*, 478(2268):20220270, 2022.
 - [30] Phanisri P Pratapa, Ke Liu, and Glaucio H Paulino. Geometric mechanics of origami patterns exhibiting poisson’s ratio switch by breaking mountain and valley assignment. *Physical Review Letters*, 122(15):155501, 2019.
 - [31] V Brunck, F Lechenault, A Reid, and M Adda-Bedia. Elastic theory of origami-based metamaterials. *Physical Review E*, 93(3):033005, 2016.
 - [32] Deanna Sessions, Alexander Cook, Kazuko Fuchi, Andrew Gillman, Gregory Huff, and Philip Buskohl. Origami-inspired frequency selective surface with fixed frequency response under folding. *Sensors*, 19(21):4808, 2019.
 - [33] Andrew Gillman, Gregory Wilson, Kazuko Fuchi, Darren Hartl, Alexander Pankonien, and Philip Buskohl. Design of soft origami mechanisms with targeted symmetries. *Actuators*, 8(1): 3, 2018.
 - [34] Andrew S Gillman, Kazuko Fuchi, and Philip R Buskohl. Discovering sequenced origami folding through nonlinear mechanics and topology optimization. *Journal of Mechanical Design*, 141(4):041401, 2019.
 - [35] Sourabh Shende, Andrew Gillman, David Yoo, Philip Buskohl, and Kumar Vemaganti. Bayesian topology optimization for efficient design of origami folding structures. *Structural and Multidisciplinary Optimization*, 63:1907–1926, 2021.
 - [36] Munkyun Lee, Yuki Miyajima, and Tomohiro Tachi. Designing and analyzing multistable mechanisms using quadrilateral boundary rigid origami. *Journal of Mechanisms and Robotics*, 16(1):011008, 2024.
 - [37] Fan Feng, Xiangxin Dang, Richard D. James, and Paul Plucinsky. The designs and deformations of rigidly and flat-foldable origami. *Journal of the Mechanics and Physics of Solids*, page 104018, 2020. ISSN 0022-5096.
 - [38] Fan Feng, Paul Plucinsky, and Richard D James. Helical miura origami. *Physical Review E*, 101(3):033002, 2020.

- [39] Levi H Dudte, Gary PT Choi, and L Mahadevan. An additive algorithm for origami design. *Proceedings of the National Academy of Sciences*, 118(21):e2019241118, 2021.
- [40] Robert J Lang and Larry Howell. Rigidly foldable quadrilateral meshes from angle arrays. *Journal of Mechanisms and Robotics*, 10(2):021004, 2018.
- [41] Xiangxin Dang, Fan Feng, Paul Plucinsky, Richard D James, Huling Duan, and Jianxiang Wang. Inverse design of deployable origami structures that approximate a general surface. *International Journal of Solids and Structures*, 234:111224, 2022.
- [42] Charles Dorn, Robert J Lang, and Sergio Pellegrino. Kirigami tiled surfaces with multiple configurations. *Proceedings of the Royal Society A*, 478(2267):20220405, 2022.
- [43] Yang Li and Sergio Pellegrino. A theory for the design of multi-stable morphing structures. *Journal of the Mechanics and Physics of Solids*, 136:103772, 2020.
- [44] Peter Dieleman, Niek Vasmel, Scott Waitukaitis, and Martin van Hecke. Jigsaw puzzle design of pluripotent origami. *Nature Physics*, 16(1):63–68, 2020.
- [45] Huan Liu and Richard D James. Design of origami structures with curved tiles between the creases. *Journal of the Mechanics and Physics of Solids*, page 105559, 2024.
- [46] Peter Dieleman. *Origami metamaterials: design, symmetries, and combinatorics*. PhD thesis, Leiden University, 2018.
- [47] Hao Zhou, Matthew Grasinger, Philip Buskohl, and Kaushik Bhattacharya. Low energy fold paths in multistable origami structures. *International Journal of Solids and Structures*, 265:112125, 2023.
- [48] Tomohiro Tachi. Simulation of rigid origami. *Origami*, 4(08):175–187, 2009.
- [49] Yang Li. Motion paths finding for multi-degree-of-freedom mechanisms. *International Journal of Mechanical Sciences*, 185:105709, 2020.
- [50] K Fuchi, PR Buskohl, JJ Joo, GW Reich, and RA Vaia. Numerical analysis of origami structures through modified frame elements. *Origami6; Miura, K., Kawasaki, T., Tachi, T., Uehara, R., Lang, RJ, Wang-Iverson, P., Eds*, pages 385–395, 2016.
- [51] Jiayao Ma and Zhong You. Energy absorption of thin-walled square tubes with a prefolded origami pattern—part i: geometry and numerical simulation. *Journal of applied mechanics*, 81(1):011003, 2014.
- [52] Qiuting Zhang, Jonathon Wommer, Connor O’Rourke, Joseph Teitelman, Yichao Tang, Joshua Robison, Gaojian Lin, and Jie Yin. Origami and kirigami inspired self-folding for programming three-dimensional shape shifting of polymer sheets with light. *Extreme Mechanics Letters*, 11:111–120, 2017.
- [53] Andrew Gillman, Kazuko Fuchi, and Phil R Buskohl. Truss-based nonlinear mechanical analysis for origami structures exhibiting bifurcation and limit point instabilities. *International Journal of Solids and Structures*, 147:80–93, 2018.
- [54] Mark Schenk and Simon D Guest. Origami folding: A structural engineering approach. *Origami*, 5:291–304, 2011.
- [55] Ke Liu and Glaucio H Paulino. Nonlinear mechanics of non-rigid origami: an efficient computational approach. *Proceedings of the Royal Society A: Mathematical, Physical and Engineering Sciences*, 473(2206):20170348, 2017.
- [56] ET Filipov, K Liu, Tomohiro Tachi, Mark Schenk, and Glaucio H Paulino. Bar and hinge models for scalable analysis of origami. *International Journal of Solids and Structures*, 124:26–45, 2017.
- [57] ME Lee-Trimble, Ji-Hwan Kang, Ryan C Hayward, and Christian D Santangelo. Robust folding

- of elastic origami. *Soft Matter*, 18(34):6384–6391, 2022.
- [58] Yao Chen, Ruizhi Xu, Chenhao Lu, Ke Liu, Jian Feng, and Pooya Sareh. Multi-stability of the hexagonal origami hyper based on group theory and symmetry breaking. *International Journal of Mechanical Sciences*, 247:108196, 2023.
- [59] Bryan Gin-ge Chen and Christian D Santangelo. Branches of triangulated origami near the unfolded state. *Physical Review X*, 8(1):011034, 2018.
- [60] James McInerney, Bryan Gin-ge Chen, Louis Theran, Christian D Santangelo, and D Zeb Rocklin. Hidden symmetries generate rigid folding mechanisms in periodic origami. *Proceedings of the National Academy of Sciences*, 117(48):30252–30259, 2020.
- [61] sarah belcastro and Thomas C Hull. Modelling the folding of paper into three dimensions using affine transformations. *Linear Algebra and its applications*, 348(1-3):273–282, 2002.
- [62] Weina Wu and Zhong You. Modelling rigid origami with quaternions and dual quaternions. *Proceedings of the Royal Society A: Mathematical, physical and engineering sciences*, 466(2119):2155–2174, 2010.
- [63] Yue Zheng, Imtiaz Niloy, Paolo Celli, Ian Tobasco, and Paul Plucinsky. Continuum field theory for the deformations of planar kirigami. *Physical Review Letters*, 128(20):208003, 2022.
- [64] Yue Zheng, I Niloy, I Tobasco, P Celli, and P Plucinsky. Modelling planar kirigami metamaterials as generalized elastic continua. *Proceedings of the Royal Society A*, 479(2272):20220665, 2023.
- [65] Hu Xu, Ian Tobasco, and Paul Plucinsky. Derivation of an effective plate theory for parallelogram origami from bar and hinge elasticity. *arXiv preprint arXiv:2311.10870*, 2023.
- [66] David A. Huffman. Curvature and creases: A primer on paper. *IEEE Transactions on computers*, (10):1010–1019, 1976.
- [67] Brandon H Hanna, Jason M Lund, Robert J Lang, Spencer P Magleby, and Larry L Howell. Waterbomb base: a symmetric single-vertex bistable origami mechanism. *Smart Materials and Structures*, 23(9):094009, 2014.
- [68] Brandon H Hanna, Spencer P Magleby, Robert J Lang, and Larry L Howell. Force–deflection modeling for generalized origami waterbomb-base mechanisms. *Journal of Applied Mechanics*, 82(8), 2015.
- [69] Huan Liu, Paul Plucinsky, Fan Feng, and Richard D James. Origami and materials science. *Philosophical Transactions of the Royal Society A*, 379(2201):20200113, 2021.
- [70] Richard D James. Objective structures. *Journal of the Mechanics and Physics of Solids*, 54(11):2354–2390, 2006.
- [71] Riccardo Foschi, Thomas C Hull, and Jason S Ku. Explicit kinematic equations for degree-4 rigid origami vertices, euclidean and non-euclidean. *Physical Review E*, 106(5):055001, 2022.
- [72] Johnna Farnham, Thomas C Hull, and Aubrey Rumbolt. Rigid folding equations of degree-6 origami vertices. *Proceedings of the Royal Society A*, 478(2260):20220051, 2022.
- [73] Erik D Demaine, Martin L Demaine, Vi Hart, Gregory N Price, and Tomohiro Tachi. (non) existence of pleated folds: how paper folds between creases. *Graphs and Combinatorics*, 27:377–397, 2011.
- [74] Ke Liu, Tomohiro Tachi, and Glaucio H Paulino. Invariant and smooth limit of discrete geometry folded from bistable origami leading to multistable metasurfaces. *Nature communications*, 10(1):4238, 2019.
- [75] Wolfram Research, Inc. Mathematica, Version 13.3. URL <https://www.wolfram.com/mathematica>. Champaign, IL, 2023.

- [76] Alden Yellowhorse, Robert J Lang, Kyler Tolman, and Larry L Howell. Creating linkage permutations to prevent self-intersection and enable deployable networks of thick-origami. *Scientific reports*, 8(1):12936, 2018.
- [77] Robert J Lang, Kyler A Tolman, Erica B Crampton, Spencer P Magleby, and Larry L Howell. A review of thickness-accommodation techniques in origami-inspired engineering. *Applied Mechanics Reviews*, 70(1):010805, 2018.
- [78] Yan Chen, Rui Peng, and Zhong You. Origami of thick panels. *Science*, 349(6246):396–400, 2015.
- [79] Yi Zhu and Evgueni T Filipov. Large-scale modular and uniformly thick origami-inspired adaptable and load-carrying structures. *Nature Communications*, 15(1):2353, 2024.
- [80] Yi Zhu and Evgueni T Filipov. An efficient numerical approach for simulating contact in origami assemblages. *Proceedings of the Royal Society A*, 475(2230):20190366, 2019.
- [81] Tomas Möller and Ben Trumbore. Fast, minimum storage ray/triangle intersection. In *ACM SIGGRAPH 2005 Courses*, pages 7–es. 2005.